EUROPEAN ORGANISATION FOR NUCLEAR RESEARCH

CERN-PH-EP/2005-014
21 February 2005
Revised xx June 2005

Measurement of the running of the QED coupling in small-angle Bhabha scattering at LEP

OPAL Collaboration

Abstract

Using the OPAL detector at LEP, the running of the effective QED coupling $\alpha(t)$ is measured for space-like momentum transfer from the angular distribution of small-angle Bhabha scattering. In an almost ideal QED framework, with very favourable experimental conditions, we obtain:

$$\Delta\alpha(-6.07\,\mathrm{GeV}^2) - \Delta\alpha(-1.81\,\mathrm{GeV}^2) = (440 \pm 58 \pm 43 \pm 30) \times 10^{-5}\,,$$

where the first error is statistical, the second is the experimental systematic and the third is the theoretical uncertainty. This agrees with current evaluations of $\alpha(t)$. The null hypothesis that α remains constant within the above interval of $-t$ is excluded with a significance above $5\,\sigma$. Similarly, our results are inconsistent at the level of $3\,\sigma$ with the hypothesis that only leptonic loops contribute to the running. This is currently the most significant direct measurement of the increase of the effective QED coupling strength with increasing momentum transfer.

Submitted to European Physical Journal C

The OPAL Collaboration

G. Abbiendi[2], C. Ainsley[5], P.F. Åkesson[3,y], G. Alexander[22], G. Anagnostou[1], K.J. Anderson[9], S. Asai[23], D. Axen[27], I. Bailey[26], E. Barberio[8,p], T. Barillari[32], R.J. Barlow[16], R.J. Batley[5], P. Bechtle[25], T. Behnke[25], K.W. Bell[20], P.J. Bell[1], G. Bella[22], A. Bellerive[6], G. Benelli[4], S. Bethke[32], O. Biebel[31], O. Boeriu[10], P. Bock[11], M. Boutemeur[31], S. Braibant[2], R.M. Brown[20], H.J. Burckhart[8], S. Campana[4], P. Capiluppi[2], R.K. Carnegie[6], A.A. Carter[13], J.R. Carter[5], C.Y. Chang[17], D.G. Charlton[1], C. Ciocca[2], A. Csilling[29], M. Cuffiani[2], S. Dado[21], G.M. Dallavalle[2], A. De Roeck[8], E.A. De Wolf[8,s], K. Desch[25], B. Dienes[30], J. Dubbert[31], E. Duchovni[24], G. Duckeck[31], I.P. Duerdoth[16], E. Etzion[22], F. Fabbri[2], P. Ferrari[8], F. Fiedler[31], I. Fleck[10], M. Ford[16], A. Frey[8], P. Gagnon[12], J.W. Gary[4], C. Geich-Gimbel[3], G. Giacomelli[2], P. Giacomelli[2], R. Giacomelli[2], M. Giunta[4], J. Goldberg[21], E. Gross[24], J. Grunhaus[22], M. Gruwé[8], P.O. Günther[3], A. Gupta[9], C. Hajdu[29], M. Hamann[25], G.G. Hanson[4], A. Harel[21], M. Hauschild[8], C.M. Hawkes[1], R. Hawkings[8], R.J. Hemingway[6], G. Herten[10], R.D. Heuer[25], J.C. Hill[5], D. Horváth[29,c], P. Igo-Kemenes[11], K. Ishii[23], H. Jeremie[18], P. Jovanovic[1], T.R. Junk[6,i], J. Kanzaki[23,u], D. Karlen[26], K. Kawagoe[23], T. Kawamoto[23], R.K. Keeler[26], R.G. Kellogg[17], B.W. Kennedy[20], S. Kluth[32], T. Kobayashi[23], M. Kobel[3], S. Komamiya[23], T. Krämer[25], P. Krieger[6,l], J. von Krogh[11], T. Kuhl[25], M. Kupper[24], G.D. Lafferty[16], H. Landsman[21], D. Lanske[14], D. Lellouch[24], J. Letts[o], L. Levinson[24], J. Lillich[10], S.L. Lloyd[13], F.K. Loebinger[16], J. Lu[27,w], A. Ludwig[3], J. Ludwig[10], W. Mader[3,b], S. Marcellini[2], A.J. Martin[13], T. Mashimo[23], P. Mättig[m], J. McKenna[27], R.A. McPherson[26], F. Meijers[8], W. Menges[25], F.S. Merritt[9], H. Mes[6,a], N. Meyer[25], A. Michelini[2], S. Mihara[23], G. Mikenberg[24], D.J. Miller[15], W. Mohr[10], T. Mori[23], A. Mutter[10], K. Nagai[13], I. Nakamura[23,v], H. Nanjo[23], H.A. Neal[33], R. Nisius[32], S.W. O'Neale[1,*], A. Oh[8], M.J. Oreglia[9], S. Orito[23,*], C. Pahl[32], G. Pásztor[4,g], J.R. Pater[16], J.E. Pilcher[9], J. Pinfold[28], D.E. Plane[8], O. Pooth[14], M. Przybycień[8,n], A. Quadt[3], K. Rabbertz[8,r], C. Rembser[8], P. Renkel[24], J.M. Roney[26], A.M. Rossi[2], Y. Rozen[21], K. Runge[10], K. Sachs[6], T. Saeki[23], E.K.G. Sarkisyan[8,j], A.D. Schaile[31], O. Schaile[31], P. Scharff-Hansen[8], J. Schieck[32], T. Schörner-Sadenius[8,z], M. Schröder[8], M. Schumacher[3], R. Seuster[14,f], T.G. Shears[8,h], B.C. Shen[4], P. Sherwood[15], A. Skuja[17], A.M. Smith[8], R. Sobie[26], S. Söldner-Rembold[16], F. Spano[9], A. Stahl[3,x], D. Strom[19], R. Ströhmer[31], S. Tarem[21], M. Tasevsky[8,s], R. Teuscher[9], M.A. Thomson[5], E. Torrence[19], D. Toya[23], P. Tran[4], I. Trigger[8], Z. Trócsányi[30,e], E. Tsur[22], M.F. Turner-Watson[1], I. Ueda[23], B. Ujvári[30,e], C.F. Vollmer[31], P. Vannerem[10], R. Vértesi[30,e], M. Verzocchi[17], H. Voss[8,q], J. Vossebeld[8,h], C.P. Ward[5], D.R. Ward[5], P.M. Watkins[1], A.T. Watson[1], N.K. Watson[1], P.S. Wells[8], T. Wengler[8], N. Wermes[3], G.W. Wilson[16,k], J.A. Wilson[1], G. Wolf[24], T.R. Wyatt[16], S. Yamashita[23], D. Zer-Zion[4], L. Zivkovic[24]

[1]School of Physics and Astronomy, University of Birmingham, Birmingham B15 2TT, UK
[2]Dipartimento di Fisica dell' Università di Bologna and INFN, I-40126 Bologna, Italy
[3]Physikalisches Institut, Universität Bonn, D-53115 Bonn, Germany
[4]Department of Physics, University of California, Riverside CA 92521, USA
[5]Cavendish Laboratory, Cambridge CB3 0HE, UK
[6]Ottawa-Carleton Institute for Physics, Department of Physics, Carleton University, Ottawa,

Ontario K1S 5B6, Canada
[8]CERN, European Organisation for Nuclear Research, CH-1211 Geneva 23, Switzerland
[9]Enrico Fermi Institute and Department of Physics, University of Chicago, Chicago IL 60637, USA
[10]Fakultät für Physik, Albert-Ludwigs-Universität Freiburg, D-79104 Freiburg, Germany
[11]Physikalisches Institut, Universität Heidelberg, D-69120 Heidelberg, Germany
[12]Indiana University, Department of Physics, Bloomington IN 47405, USA
[13]Queen Mary and Westfield College, University of London, London E1 4NS, UK
[14]Technische Hochschule Aachen, III Physikalisches Institut, Sommerfeldstrasse 26-28, D-52056 Aachen, Germany
[15]University College London, London WC1E 6BT, UK
[16]Department of Physics, Schuster Laboratory, The University, Manchester M13 9PL, UK
[17]Department of Physics, University of Maryland, College Park, MD 20742, USA
[18]Laboratoire de Physique Nucléaire, Université de Montréal, Montréal, Québec H3C 3J7, Canada
[19]University of Oregon, Department of Physics, Eugene OR 97403, USA
[20]CCLRC Rutherford Appleton Laboratory, Chilton, Didcot, Oxfordshire OX11 0QX, UK
[21]Department of Physics, Technion-Israel Institute of Technology, Haifa 32000, Israel
[22]Department of Physics and Astronomy, Tel Aviv University, Tel Aviv 69978, Israel
[23]International Centre for Elementary Particle Physics and Department of Physics, University of Tokyo, Tokyo 113-0033, and Kobe University, Kobe 657-8501, Japan
[24]Particle Physics Department, Weizmann Institute of Science, Rehovot 76100, Israel
[25]Universität Hamburg/DESY, Institut für Experimentalphysik, Notkestrasse 85, D-22607 Hamburg, Germany
[26]University of Victoria, Department of Physics, P O Box 3055, Victoria BC V8W 3P6, Canada
[27]University of British Columbia, Department of Physics, Vancouver BC V6T 1Z1, Canada
[28]University of Alberta, Department of Physics, Edmonton AB T6G 2J1, Canada
[29]Research Institute for Particle and Nuclear Physics, H-1525 Budapest, P O Box 49, Hungary
[30]Institute of Nuclear Research, H-4001 Debrecen, P O Box 51, Hungary
[31]Ludwig-Maximilians-Universität München, Sektion Physik, Am Coulombwall 1, D-85748 Garching, Germany
[32]Max-Planck-Institute für Physik, Föhringer Ring 6, D-80805 München, Germany
[33]Yale University, Department of Physics, New Haven, CT 06520, USA

[a] and at TRIUMF, Vancouver, Canada V6T 2A3
[b] now at University of Iowa, Dept of Physics and Astronomy, Iowa, U.S.A.
[c] and Institute of Nuclear Research, Debrecen, Hungary
[e] and Department of Experimental Physics, University of Debrecen, Hungary
[f] and MPI München
[g] and Research Institute for Particle and Nuclear Physics, Budapest, Hungary
[h] now at University of Liverpool, Dept of Physics, Liverpool L69 3BX, U.K.
[i] now at Dept. Physics, University of Illinois at Urbana-Champaign, U.S.A.
[j] and Manchester University Manchester, M13 9PL, United Kingdom
[k] now at University of Kansas, Dept of Physics and Astronomy, Lawrence, KS 66045, U.S.A.
[l] now at University of Toronto, Dept of Physics, Toronto, Canada
[m] current address Bergische Universität, Wuppertal, Germany
[n] now at University of Mining and Metallurgy, Cracow, Poland

[o] now at University of California, San Diego, U.S.A.
[p] now at The University of Melbourne, Victoria, Australia
[q] now at IPHE Université de Lausanne, CH-1015 Lausanne, Switzerland
[r] now at IEKP Universität Karlsruhe, Germany
[s] now at University of Antwerpen, Physics Department,B-2610 Antwerpen, Belgium; supported by Interuniversity Attraction Poles Programme – Belgian Science Policy
[u] and High Energy Accelerator Research Organisation (KEK), Tsukuba, Ibaraki, Japan
[v] now at University of Pennsylvania, Philadelphia, Pennsylvania, USA
[w] now at TRIUMF, Vancouver, Canada
[x] now at DESY Zeuthen
[y] now at CERN
[z] now at DESY
[*] Deceased

1 Introduction

The electromagnetic coupling constant is a basic parameter of the Standard Model, known with a relative precision of 4×10^{-9} [1] at zero momentum transfer. In QED the effective coupling changes, or *runs*, with the scale of momentum transfer due to vacuum polarization. This is due to virtual lepton and quark loop corrections to the photon propagator. This effect can also be understood as an increasing penetration of the polarized cloud of virtual particles which screen the bare electric charge of a particle as it is probed at smaller and smaller distance. The effective QED coupling is generally expressed as:

$$\alpha(q^2) = \frac{\alpha_0}{1 - \Delta\alpha(q^2)} \tag{1}$$

where $\alpha_0 = \alpha(q^2 = 0) \simeq 1/137.036$ is the fine structure constant and q^2 is the momentum transfer squared of the exchanged photon.

While the leptonic contributions to $\Delta\alpha$ are calculable to very high accuracy, the hadronic ones are more problematic as they involve quark masses and hadronic physics at low momentum scales. The hadronic contribution can be evaluated through a dispersion integral over the measured cross section of $e^+e^- \to$ hadrons, supplemented with perturbative QCD at energies above the resonance region [2,3]. The main difficulty of this approach comes from the integration of experimental data in the region of hadronic resonances, which gives the dominant uncertainty on $\Delta\alpha$. The effective QED coupling $\alpha(q^2)$ is an essential ingredient for many precision physics predictions. It contributes one of the dominant uncertainties in the electroweak fits constraining the Higgs mass [4]. There are also many evaluations which are more theory-driven, extending the application of perturbative QCD down to about 2 GeV, for example [5]. An alternative approach uses the Adler function [6] and perturbative QCD in the negative q^2 (*space-like*) region [7], where $\Delta\alpha$ is a smooth function.

Precise measurements of the muon anomalous magnetic moment [8, 9] have stringently tested vacuum polarization corrections to the photon propagator, due not only to electrons but also to other leptons and hadronic states. Due to their very high precision, such measurements

currently constitute a stringent overall test of the Standard Model, in which many classes of radiative corrections are probed, involving electromagnetic, strong and weak interactions. They also have sensitivity to potential physics beyond the Standard Model. Vacuum polarization corrections affect the muon anomaly when integrated over virtual photon states encompassing a wide range of both positive and negative q^2. In contrast, in this analysis, we present a *direct* measurement of the running of the electromagnetic coupling in the space-like region, where by direct we mean that the change in the effective electromagnetic coupling strength is probed for photon propagators of distinctly different q^2.

There have been only a few direct observations of the running of the QED coupling [10,11,12,13]. Most of these analyses involve measurements of cross sections and their ratios and obtain values of $\alpha(q^2)$ which are found to deviate from α_0 or from the assumed value of the coupling at some initial scale. Theoretical uncertainties on the predicted absolute cross sections as well as experimental scale errors can influence such determinations or reduce their significance. The TOPAZ [10] and the OPAL [11] experiments probed the running in the *time-like* region (positive q^2) from e^+e^- annihilations to leptonic final states. Far enough from the Z resonance these processes are dominated by single photon exchange, although they substantially involve the full electroweak theory. Large-angle Bhabha scattering has been studied by the VENUS [12] and L3 [13] experiments to measure the running in the space-like region. In this case both s- and t-channel γ-exchange diagrams are important and the effective QED coupling appears as a function of s or t respectively. Moreover, interference contributions due to Z-exchange are also sizeable.

In this paper we measure the running of α in the space-like region, by studying the angular dependence of small-angle Bhabha scattering using data collected by the OPAL detector at LEP. Small-angle Bhabha scattering appears to be an ideal process for a direct measurement of the running of α since the process is dominated by the exchange of a single photon where the momentum transfer squared t is simply related to the polar scattering angle. The angular distribution is modified by the running coupling which appears as $\alpha^2(t)$. There has been only one similar previous study by the L3 experiment [13].

We confine ourselves to the small angular region used for the luminosity measurement, which approximately corresponds to $2 \leq -t \leq 6$ GeV^2 at centre-of-mass energies near the Z resonance peak (LEP 1). At this t scale the average $\Delta\alpha$ is about 2%. The number of small-angle Bhabha events is used to determine the integrated luminosity, so that we will not make an absolute measurement of $\alpha(t)$; rather we will look only at the variation of $\Delta\alpha$ across the acceptance, which is expected to be about 0.5%, leading to an observable effect of about 1%. An interesting property of this low $|t|$ region is that, although the absolute $\Delta\alpha$ value is dominated by the leptonic contributions, the leptonic and hadronic components contribute about equally to its variation across the region accessible to our measurements.

A crucial element in this work has been the very high precision in measuring the scattering angle provided by the OPAL Silicon-Tungsten (SiW) luminometer [14]. Among the experimental advantages are also the high available statistics and the purity of the data sample. Not less important is the cleanliness of this kind of measurement from a theoretical point of view, as has been pointed out recently in [15]. Small-angle Bhabha scattering is strongly dominated by single-photon t-channel exchange, while s-channel photon exchange is practically negligible. The cross section is currently exactly calculable up to the leading $\mathcal{O}(\alpha^2)$ terms in the QED photonic corrections (herein indicated as $\mathcal{O}(\alpha^2 L^2)$, where $L = \ln(|t|/m_e^2) - 1$ is the large log-

arithm). Many existing calculations are described in [16] and were also widely cross-checked, mainly to reduce the theoretical error on the determination of the luminosity at LEP 1. Higher order terms are partially accounted for through exponentiation. A calculation accurate to the subleading $\mathcal{O}(\alpha^2)$ terms [17] also exists. Corrections for Z interference are very small and well known, so that small-angle Bhabha scattering near the Z pole can be considered an essentially pure QED process. A comparison of data with such precise calculations can determine the value of the effective QED coupling in the most accurate way without relying on the correctness of the SU(2)×U(1) electroweak model.

The paper is organized as follows: we explain the analysis method in Section 2, the detector and its Monte Carlo simulation are briefly described in Section 3 and the event selection in Section 4. The procedure to correct the data distributions is explained in Section 5 and checked in Section 6. The experimental systematic uncertainties are described in detail in Section 7. The theoretical uncertainties are discussed in Section 8. The results are finally given in Section 9, and a concluding summary in Section 10.

2 Analysis method

The Bhabha differential cross section can be written in the following form for small scattering angle:

$$\frac{\mathrm{d}\sigma}{\mathrm{d}t} = \frac{\mathrm{d}\sigma^{(0)}}{\mathrm{d}t}\left(\frac{\alpha(t)}{\alpha_0}\right)^2 (1+\epsilon)\ (1+\delta_\gamma) + \delta_\mathrm{Z} \tag{2}$$

where

$$\frac{\mathrm{d}\sigma^{(0)}}{\mathrm{d}t} = \frac{4\pi\alpha_0^2}{t^2} \tag{3}$$

is the Born term for t-channel single photon exchange, α_0 is the fine structure constant and $\alpha(t)$ is the effective coupling at the momentum transfer scale t. Here ϵ represents the radiative corrections to the Born cross section, while δ_γ and δ_Z are respectively the contributions of photon and Z s-channel exchange, both dominated by interference with t-channel photon exchange. The contributions of δ_γ and δ_Z are much smaller than those of ϵ and the vacuum polarization. Therefore, with a precise knowledge of the radiative corrections (ϵ term) one can determine the effective coupling $\alpha(t)$ by measuring the differential cross section. The form of Equation (2) is an approximation since the δ_γ term is not strictly factorizable with the effective coupling $\alpha^2(t)$. In fact the s-channel amplitude couples as $\alpha(s)$, where s is the centre-of-mass energy squared. The practical validity of Equation (2) is a consequence of the smallness of the δ_γ term, which could even be neglected.

The counting rate of Bhabha events in the SiW luminometers is used to determine the integrated luminosity, so that we cannot make an absolute measurement of $\alpha(t)$ without an independent determination of the luminosity. Instead, the structure of the cross section as written in Equation (2) easily allows the variation of $\alpha(t)$ over the accessible t range to be determined, since the dominant contribution to the cross section contains the factor $(\alpha(t)/\alpha_0)^2$. At leading order the variable t is simply related to the scattering angle, θ:

$$t = -s\,\frac{1-\cos\theta}{2} \approx -\frac{s\,\theta^2}{4}\,. \tag{4}$$

Photon radiation (in particular initial-state radiation) smears this correspondence. The event selection that we use, described in Section 4, has been carefully chosen to reduce the impact of radiative events. In particular the energy cuts and the acollinearity cut are very effective. As a result the event sample is strongly dominated by two-cluster configurations, with almost full energy back-to-back scattered e^+ and e^-. For such a selection Equation (4) represents a good approximation. The scattering angle is measured from the radial position R of the scattered e^+ and e^- at reference planes located within the SiW luminometers, at a distance z from the interaction point:

$$\tan\theta = R/z\,. \tag{5}$$

We use the BHLUMI [18] Monte Carlo generator for all calculations of small-angle Bhabha scattering. It is a multiphoton exponentiated generator accurate up to the leading logarithmic $\mathcal{O}(\alpha^2 L^2)$ terms. Higher order photonic contributions are partially included by virtue of the exponentiation. The generated events always contain the scattered electron and positron plus an arbitrary number of (non-collinear) photons. Small contributions from s-channel photon exchange and Z interference are also included. Corrections due to vacuum polarization are implemented with a few choices for the parameterization of the hadronic term [2,19]. We used the option to generate weighted events, such that we could access all the available intermediate weights which contribute to the final complete cross section event by event. In particular we could also modify the parameterization of the vacuum polarization or set $\alpha(t) \equiv \alpha_0$ to assume a fixed coupling α_0.

We compare the radial distribution of the data (and hence the t-spectrum) with the predictions of the BHLUMI Monte Carlo to determine the running of α within the accepted region. If the Monte Carlo is modified by setting the coupling to the constant value $\alpha(t) \equiv \alpha_0$, the ratio f of the number of data to Monte Carlo events in a given radial bin is:

$$f(t) = \frac{N_{\rm data}(t)}{N^0_{\rm MC}(t)} \propto \left(\frac{1}{1-\Delta\alpha(t)}\right)^2 . \tag{6}$$

The dominant dependence of $\Delta\alpha(t)$ expected from theory is logarithmic. We therefore fitted the ratio $f(t)$ as:

$$f(t) = a + b\,\ln\left(\frac{t}{t_0}\right) \tag{7}$$

where $t_0 = -3.3$ GeV^2 is chosen to be close to the mean value of t in the data sample. The value of t in each bin is calculated according to Equation (4), averaged over the bin, assuming the cross section dependence of Equation (3). The parameter a ($a \approx 1$) is not relevant since the Monte Carlo is normalized to the data. The slope b represents the full observable effect of the running of $\alpha(t)$, both the leptonic and hadronic components. It is related to the variation of the coupling by:

$$\Delta\alpha(t_2) - \Delta\alpha(t_1) \simeq \frac{b}{2}\,\ln\left(\frac{t_2}{t_1}\right) \tag{8}$$

where t_1 and t_2 correspond to the acceptance limits. The errors associated with these approximations are negligible, and discussed in Section 7.9.

With the acceptance cuts specified in Section 4 and the average centre-of-mass energy $\sqrt{s} =$ 91.2208 GeV, the reference t range is: $t_1 = -1.81$ GeV^2, $t_2 = -6.07$ GeV^2, $\ln(t_2/t_1) = 1.21$.

The expected value of the effective slope in this t range is $b = 0.00761$, determined by using the Burkhardt-Pietrzyk parameterization [3] of the hadronic contributions.

It is important to realize which systematic effects could mimic the expected running or disturb the measurement. The most potentially harmful effects are biases in the radial coordinate. Most simply one could think of dividing the detector acceptance into two and determining the slope using only two bins. In such a model the running is equivalent to a bias in the central division of 70 μm. Biases on the inner or outer radial cut have a little less importance and could mimic the full running for 90 or 210 μm systematic offsets respectively. Concerning radial metrology, a uniform bias of 0.5 mm on all radii would give the same observable slope as the expected running. Knowledge of the beam parameters, particularly the transverse offset and the beam divergence, is also quite important.

3 Detector, data samples and Monte Carlo simulation

The OPAL detector and trigger have been described in detail elsewhere [20]. In particular this analysis is based on the silicon-tungsten luminometer (SiW), which was used to determine the luminosity from the counting rate of accepted Bhabha events from 1993 until the end of LEP running. The SiW was designed to improve the precision of the luminosity measurement to better than 1 per mille. In fact it achieved a fractional experimental systematic error of 3.4×10^{-4}. The detector and the luminosity measurement are extensively described in [14]. Here we only briefly review the detector aspects relevant for this analysis.

The OPAL SiW luminometer consists of 2 identical cylindrical calorimeters, encircling the beam pipe symmetrically at about ± 2.5 m from the interaction point. Each calorimeter is a stack of 19 silicon layers interleaved with 18 tungsten plates, with a sensitive depth of 14 cm, representing 22 radiation lengths (X_0). The first 14 tungsten plates are each $1\,X_0$ thick, while the last 4 are each $2\,X_0$ thick. The sensitive area fully covers radii between 6.2 and 14.2 cm from the beam axis. Each detector layer is segmented with R-ϕ geometry in a 32×32 pad array. The pad size is 2.5 mm radially and 11.25 degrees in azimuth. In total the whole luminometer has 38,912 readout channels corresponding to the individual silicon pads. The calibration was studied with electrical pulses generated both on the readout chips and on the front-end boards, as well as with ionization signals generated in the silicon using test beams and laboratory sources. Overall pad-to-pad gain variations were within 1%. Particles originating at the interaction point had to traverse the material constituting the beam pipe and its support structures as well as cables from inner detector components before reaching the face of the SiW calorimeters. The distribution of this material upstream of the calorimeters is shown in Fig. 1. The material thickness was kept at a minimum especially in the crucial region of the inner acceptance cut where it amounts to about $0.25\,X_0$, while in the middle of the acceptance it increases to about $2\,X_0$. The model used for the calculation of the material thickness only approximates the actual situation, and dictates our strategy of determining the material effects from the data, using the figure as an approximate guide. Controlling and correcting the possible biases in the reconstructed position caused by this material was one of the most important aspects of this analysis and is addressed in the following sections.

We use the data samples collected in 1993-95 at energies close to the Z resonance peak. In total they amount to 101 pb^{-1} of OPAL data, corresponding to 12.0×10^6 accepted small-angle

Bhabha events. In 1993 and 1995, energy scans were performed and data were taken at three energy points: close to the Z peak and approximately 1.8 GeV above and below it. In 1994 all data were taken near the Z peak. We divide the data into nine subsamples, depending on the year, the centre-of-mass energy and the running conditions, such as the beam parameters, in the same way as for the luminosity analysis [14]. The same notation is also used for labelling the subsamples. One subsample at peak energy (94-b) includes 40% of the total number of events, while the remaining statistics are divided roughly equally among the other, smaller, subsamples. When LEP 2 data-taking started in 1996 the detector configuration changed, with the installation of tungsten shields designed to protect the inner tracking detectors from synchrotron radiation. These introduced about 50 radiation lengths of material in front of the calorimeters between 26 and 33 mrad from the beam axis, thus reducing the useful acceptance of the detector at the lower polar angle limit. Moreover the new fiducial acceptance cut fell right in the middle of the previous acceptance, where the preshowering material was maximum. For these reasons we have limited this analysis to the LEP 1 data samples.

The OPAL SiW detector simulation does not rely on a detailed physical simulation of electromagnetic showers in the detector. Instead it is based on a parameterization of the detector response obtained from the data [14]. This approach gives a much more reliable description of the tails of the detector response functions, which are primarily due to extreme fluctuations in shower development, than we could obtain using any existing program which attempts to simulate the basic interactions of electrons and photons in matter. The measured LEP beam size and divergence, as well as the measured offset and tilt of the beam with respect to the calorimeters, are also incorporated into this simulation. The Monte Carlo simulation is used to correct the acceptance for the effects of the detector energy response, the coordinate resolution and LEP beam parameters. Corresponding to each data subsample we generated an independent sample of BHLUMI events, using a slightly different set of parameters to match the experimental conditions in each case. The statistics were always at least 10 times those of the corresponding data set.

There are other effects which are not accounted for by the Monte Carlo simulation, but rather studied directly in data. These include accidental background, detector metrology and, most importantly, biases in the reconstructed radial coordinate. The latter is crucial for this analysis and will be discussed in Section 5.

4 Event selection

The event selection criteria can be classified into *isolation* cuts, which isolate a sample of pure Bhabha scattering events from the off-momentum background, and acceptance defining, or *definition* cuts. The isolation cuts are used to define a fiducial set of events which lie within the good acceptance of both calorimeters and are essentially background free. The definition cuts then select subsets of events from within the fiducial sample.

Showers generated by incident electrons and photons are recognized as clusters in the calorimeters and their energies and coordinates determined. The fine segmentation of the detectors allows incident particles with separations greater than 1 cm to be individually reconstructed with good efficiency.

The coordinate system used throughout this paper is cylindrical, with the z-axis pointing along the direction of the electron beam, passing through the centres of the two calorimeter bores. The origin of the azimuthal coordinate, ϕ, is in the horizontal plane, towards the inside of the LEP ring. All radial coordinate measurements are projected onto reference planes at a distance of ± 246.0225 cm from the nominal intersection point. These reference planes correspond to the nominal position of the silicon layers $7\,X_0$ deep in the two calorimeters (hereafter we will identify the relevant layers with expressions like *layer* 7 or *layer* $7\,X_0$ without distinction).

The *isolation* cuts consist of the following requirements, imposed on (R_R,ϕ_R) and (R_L,ϕ_L), the radial and azimuthal coordinates of the highest energy cluster associated with the Bhabha event, in each of the Right and Left calorimeters, and on E_R and E_L, the total fiducial energy deposited by the Bhabha event in each of the two calorimeters, explicitly including any detected energy of radiated photons:

- Loose radial cut, Right (Left)
$$6.7 \text{ cm} < R_R < 13.7 \text{ cm}$$
$$(6.7 \text{ cm} < R_L < 13.7 \text{ cm})$$
- Acoplanarity cut
$$||\phi_R - \phi_L| - \pi| < 200 \text{ mrad}$$
- Acollinearity cut
$$|\Delta R| = |R_R - R_L| < 2.5 \text{ cm}$$
- Minimum energy cut, Right (Left)
$$E_R > 0.5 \cdot E_{beam}$$
$$(E_L > 0.5 \cdot E_{beam})$$
- Average energy cut
$$(E_R + E_L)/2 > 0.75 \cdot E_{beam}$$

Note that by defining the energy cuts relative to the beam energy, E_{beam}, the selection efficiency is largely independent of $\sqrt{s}$.

The acollinearity cut (which corresponds to approximately 10.4 mrad) is introduced in order to ensure that the acceptance for single radiative events is effectively determined geometrically and not by the explicit energy cuts.

The isolation cuts accept events in which the radial coordinate, on both the Right and the Left side, is more than two pad widths (0.5 cm) away from the edge of the sensitive area of the detector. The *definition* cuts, based solely on the reconstructed radial positions (R_R, R_L) of the two highest energy clusters, then require the radial position on one side or the other to be at least two further pads towards the inside of the acceptance. The Right and Left definition cuts are chosen so as to correspond closely to radial pad boundaries in a given detector layer. When the chosen layer is the reference layer at $7\,X_0$, the definition cuts are:

- Right side
$$7.2 \text{ cm} < R_R < 13.2 \text{ cm}$$
- Left side
$$7.2 \text{ cm} < R_L < 13.2 \text{ cm}$$

Expressed in terms of polar angles, these cuts correspond to 29.257 and 53.602 mrad.

The measured radial distribution of Bhabha events will later be corrected with the procedure explained in Section 5. This is based on one specific silicon layer, which can be varied with some freedom. After a given layer is chosen, the acceptance cuts and all the radial bin boundaries are

defined according to its pad boundaries, to match most closely with the correction procedure. For example, when using the layer at $4\,X_0$, the minimum and maximum radii become 7.2584 cm and 13.3071 cm.

The radial distributions after the isolation cuts are shown in Fig. 2 for the complete data statistics and compared to Monte Carlo distributions normalized to the same number of events. The agreement is good except in the central part, where effects from the preshowering material are expected. Their correction is described in the following section.

The acceptance specified by the definition cuts is 0.5 cm (corresponding to two radial pad widths) wider than that used to define the OPAL luminosity [14]. In this way we extend the lever arm for observation of the running of α. The compatibility of the added data is quite good as can be seen from Fig. 2, where each point corresponds to one pad width. The agreement has been quantified by determining the χ^2 increase obtained when the fit in the former default acceptance is extended by 2 or 3 pads at both the inner and outer radius. The $\Delta\chi^2$ is consistent with purely statistical fluctuations corresponding to the added degrees of freedom.

5 Radial coordinate anchoring

We exploit the fine radial and longitudinal granularity of the detector to produce precise and continuous radial shower coordinates. Limiting and quantifying the systematic error in these reconstructed coordinates is crucial to the current measurement. The key to ensuring that the reconstruction does not depart from the absolute physical geometry of the Si pads, especially behind the appreciable preshowering material which obscures the middle portion of the acceptance, is to study the radial coordinate as a function of depth, using each of the many layers of the detector independently. We refer to this procedure as *anchoring*. Details of how the coordinates are formed from the recorded pad information are found in [14], which should be consulted for a full understanding, but the essentials are as follows. First the smoothed radial coordinate is constructed:

- In each layer, the triplet of pads centred around the peak of the shower profile is used to form a continuous radial coordinate for the shower in that layer. The algorithm preserves two symmetry conditions, which hold to a good approximation. First, if the two largest pad signals in the triplet are equal, the coordinate falls on the pad boundary. Secondly, if the signals on the two extreme pads of the triplet are equal, the coordinate falls at the centre of the central pad.
- Acceptable layer coordinates in layers 2 to 10 are projected onto the reference plane of the detector, layer 7, which lies near the average longitudinal shower maximum, and averaged.
- This average coordinate is then smoothed to compensate for non-uniformities in the resolution across the pad structure of the detector. The smoothing algorithm imposes the constraint that no coordinate is allowed to cross the radius of a pad boundary in the reference layer 7.

This smoothed radial coordinate will be referred to as the *unanchored* coordinate. This coordinate, derived from the pad signals in many layers of the detector, is robust against fluctuations

in any single pad, and exhibits uniform, optimum, resolution. In averaging many layers, however, it does suffer from two inherent weaknesses: first, it does not preserve a transparent relation to the absolute geometry of any particular pad. Second, and even more important, it does not, in itself, allow the effect of the preshowering material to be studied as a function of depth.

We therefore apply the *anchoring* procedure:

- We estimate the residual bias, or *anchor*, of the smoothed radial coordinate at each pad boundary in a given layer of the detector, as explained in the following section. Here we rely on the simple symmetry condition that two adjacent pads will each have a probability of 50% for recording the larger signal for an ensemble of events where the shower axis lies on their common boundary. Having obtained the apparent displacement of the pad boundaries through this condition, we then obtain bin-by-bin acceptance corrections which will be applied to the radial distribution. We then refer to the coordinate as being *anchored*.

Note that in contrast to the unanchored coordinate, which relies on the entire detector to provide the optimum position of an individual shower, each anchor relies on the response of just two rings of radially adjacent pads, over the ensemble of showers which pass through them. Due to the cylindrical geometry of the detector, the radial coordinates of the pad boundaries, projected to the reference layer 7, have a small relative shift between adjacent layers of about 200 μm at the inner radius and about 350 μm at the outer radius, and therefore provide a dense net of benchmarks throughout the detector.

For the luminosity measurement, the anchoring procedure was essential in establishing the absolute radius of the crucial inner acceptance boundary. In the current analysis it becomes even more important, since it is used to correct the acceptance for every bin of the radial distribution, as well as to demonstrate that the effects of the preshowering material as a function of depth are under control. For this reason we discuss it here in some detail.

5.1 Anchoring corrections

As the radial position of the incoming particles is scanned across a radial pad boundary in a single layer, the probability for observing the largest pad signal above or below this boundary shifts rapidly, giving an image of the pad boundary as shown in Fig. 3. These plots are obtained from OPAL data taken in 1993-94 and refer to three radial pad boundaries in layer $4\,\mathrm{X}_0$ of the Right calorimeter. Similar plots were also made for test beam data. The pad boundary image is modelled with an error function:

$$\mathcal{E}(R; R_{\mathrm{off}}, \sigma_{\mathrm{a}}) = \int \mathrm{d}r\, \mathcal{G}(r; R, \sigma_{\mathrm{a}}) \Theta(r - R_{\mathrm{off}}) \tag{9}$$

where R is the distance from the nominal pad boundary, $\mathcal{G}(r; R, \sigma_{\mathrm{a}})$ is a Gaussian of width σ_{a} and mean R, and $\Theta(r - R_{\mathrm{off}})$ is a step function with offset R_{off} from the nominal pad boundary. The Gaussian width σ_{a} measures the radial resolution at the boundary. From Fig. 3 one can see that the width is similar at the inner and outer radius, while it is considerably greater at

the central radius. The offset $R_{\rm off}$ is found to be quite small at the inner edge while it increases to $\approx$10-20 μm at the central and the outer radius.

Despite our reliance on the basic symmetry condition of the reconstruction described in Section 5, in reality this symmetry is slightly violated due to the R-ϕ geometry of the pads, and the corresponding increase of pad area with radius. As a result, the mean position of an ensemble of showers which share energy equally between two radially adjacent pads will actually lie at a smaller radius than the pad boundary between them. The displacement between the point where the energy, on average, is equally shared, and the actual pad boundary is termed the *pad boundary bias*, $\delta R_{R\phi}$, and depends on the lateral extent of the shower. The pad boundary bias has been measured in a test beam and parameterized as a function of the apparent width of the shower, and varies from essentially zero to about 20 μm.

An additional, second order, effect also arises whenever a cut is imposed on a quantity with a steeply falling distribution, such as the radial Bhabha spectrum. An acceptance change is introduced due to the fact that more events actually on the uphill side of the cut will be measured to fall on the downhill side than vice versa. This *resolution flow*, $\delta R_{\rm res}$, is estimated to be a small (positive) additional bias, typically below 1 μm and increasing to about 8 μm in the worst case.

The total net bias in the smoothed radial coordinate, δR (also called anchor), is therefore given by:

$$\delta R = R_{\rm off} + \delta R_{R\phi} + \delta R_{\rm res} \tag{10}$$

where $R_{\rm off}$ is the observed offset of any particular pad boundary image, which may have positive or negative sign, while both $\delta R_{R\phi}$ and $\delta R_{\rm res}$ are always positive.

The anchors determined from 1993-94 data for the layers at 4 X_0 for all the pad boundaries used in the analysis are shown in Fig. 4. A similar trend is visible on the two sides, in particular the rise of the anchor from 5-10 μm at the inner edge to 20-25 μm around $R = 9$ cm. The error bars include in quadrature the systematic errors from the fit method, pad gain variations, and the assumed $1/R$ scaling and shower width dependence of the pad boundary bias as discussed in Section 7.1. The inner error bars show the statistical errors in the fit of the pad boundary images. More details on errors assigned to the anchors can be found in [14]. The anchors determined from 1995 data have similar features although with lower statistics.

The anchors have been determined separately for the two homogeneous data combinations, 1993-94 and 1995 data, because the amount of preshowering material was different in these two subsamples. A clear relation with the amount and distribution of the material upstream of the calorimeters is visible from the apparent width $\sigma_{\rm a}$ as a function of radius, as shown in Fig. 5. The noticeable difference between the Right and Left widths in 1993-94 data is due to the presence, on the Left, of cables from the OPAL microvertex detector. For 1995 data additional cables were installed on the Right side, which resulted in an almost symmetrical situation. The presence of a non-negligible amount of preshowering material in the middle of the acceptance constitutes the most delicate experimental problem for this analysis, since the anchoring procedure was developed and checked using the test beam only for the amount of preshowering material ($< 1\,X_0$) most relevant for the luminosity measurement. We have therefore made extensive checks as described in Section 5.2 and 6 to identify a broad region within the full depth of the detector where the anchoring procedure is valid, and derive our results using only the middle of this region.

To use the anchors, we do not actually correct the measured shower coordinates themselves, but rather convert the anchors to appropriate acceptance corrections. The acceptance of an individual radial bin with boundaries ($R_{\rm in},\ R_{\rm out}$) is affected by the net biases of the edges $\delta R_{\rm in},\ \delta R_{\rm out}$ determined as in Equation (10) according to the following formula, which gives the fractional acceptance variation:

$$\frac{\delta A}{A} = c_{\rm in}\ \delta R_{\rm in} - c_{\rm out}\ \delta R_{\rm out} \tag{11}$$

The coefficients $c_{\rm in}$ and $c_{\rm out}$ are derived by a simple analytical calculation assuming a $1/\theta^3$ spectrum for the angular distribution and are given by:

$$c_k = 2\,\frac{R_{\rm in}^2 R_{\rm out}^2}{(R_{\rm out}^2 - R_{\rm in}^2)\,R_k^3} \qquad k = {\rm in}, {\rm out} \tag{12}$$

The radial distribution is binned according to the nominal pad boundaries of the anchoring layer, projected onto the reference layer $7\,{\rm X}_0$. These anchoring corrections for a single 2.5 mm bin are at most 0.5% for the Right and 1.0% for the Left side in 1993-94 data and correspondingly 0.8% and 0.7% in 1995 data.

5.2 Limitations in the anchoring

Our best security against the presence of excess systematic error in the radial shower coordinate is to check for consistency between the anchored and unanchored coordinates. As already mentioned, the unanchored coordinates are robust, and derived from the signals observed on a large number of pads throughout the detector, while the anchored coordinates rest on observing equal signals, in the mean, inside and outside an individual radial pad boundary in a particular detector layer. These anchored coordinates provide reliable benchmarks throughout most of the detector, but are expected to become fragile at both very shallow and very deep layers of the calorimeters, particularly in the region of the detector obscured by significant preshowering material. Not only does the lateral shower profile broaden deep within the calorimeter, but beyond shower maximum the energy in the shower also becomes smaller. Both these effects make determination of the pad boundary transition increasingly subject to disturbance. At shallow depths, particularly behind preshowering material located considerably upstream of the detector, a shower can occasionally develop a long, asymmetric tail which can lead to a significantly non-Gaussian error in the position determined in a single layer.

The pad boundary bias was determined in the test beam behind a maximum of $0.84\,{\rm X}_0$ of preshowering material. Under such conditions, and at reasonable depths, we determined that the pad boundary bias could be adequately parameterized as a function of the apparent shower width alone. Behind greater amounts of preshowering material, the validity of this simplification may break down, and we can expect that an additional, explicit, depth dependence may become necessary to adequately describe the pad boundary bias at both very shallow and very deep layers within the calorimeter.

We therefore compared the anchored and unanchored coordinates as a function of the layer used for the anchoring to expose such effects. As expected, significant deviations are observed at both very shallow and very deep layers, particularly on the Left side in the 1993-94 data, where the preshowering material was greatest.

The reconstructed radial coordinate can be studied by comparing data with Monte Carlo as the radial acceptance cut is varied. The Monte Carlo here assumes the expected running of α and that the radial coordinate is reconstructed without bias. Thus differences in the acceptance of the data and Monte Carlo as the radial cut is varied, beyond those expected from the finite statistics and any departure from the expected running of α, can indicate biases in the radial coordinate. We indicate with $N(R_1; R_2)$ the number of events falling between radii R_1 and R_2. The acceptance change obtained by moving the inner radial cut to any given position R is then proportional to $\Delta N = N(R; R_{\rm max}) - N(R_{\rm min}; R_{\rm max})$, where $R_{\rm min} = 7.2$ cm and $R_{\rm max} = 13.2$ cm are the acceptance limits. We normalize the Monte Carlo to the data, $N_{\rm MC}(R_{\rm min}; R_{\rm max}) = N_{\rm data}(R_{\rm min}; R_{\rm max})$ and then form the quantity:

$$\left(\frac{\Delta A}{A}\right)_{\rm data} - \left(\frac{\Delta A}{A}\right)_{\rm MC} = \frac{N_{\rm data}(R; R_{\rm max}) - N_{\rm MC}(R; R_{\rm max})}{N_{\rm data}(R_{\rm min}; R_{\rm max})}. \tag{13}$$

This relative acceptance, as a function of R, is shown as a shaded band (the lower one) for the Right and the Left side selection in Fig. 6 for 1993-94 data. The width of each band represents the binomial errors with respect to the reference selection 7.2 cm $\leq R \leq$ 13.2 cm. Note that, by construction, both ends of the relative acceptance band at $R = 7.2$ cm and $R = 13.2$ cm lie at zero.

The solid points show the anchoring results for all the relevant pad boundaries in layers between $1\,{\rm X}_0$ and $10\,{\rm X}_0$. The radial bias corresponding to each anchor is converted into an acceptance variation using the formula:

$$\frac{\delta A}{A} = 2\,\frac{R_{\rm min}^2 R_{\rm max}^2}{R_{\rm max}^2 - R_{\rm min}^2}\,\frac{\delta R}{R^3} \tag{14}$$

Since the normalization is the total acceptance, the low R points have a greater influence in the plot, due to the $1/R^3$ weighting. Therefore any visible structure tends to be flattened at increasing radius. Any of the anchors can be chosen to fix the absolute offset in the continuous radial coordinate. Here we choose the anchor at $R = 7.2$ cm in layer $7\,{\rm X}_0$ and this point correspondingly lies at zero.

Each group of nearby points, marked by either circles or triangles, refers to a given radial pad boundary, and the individual points in each group to different layers, at variable depth in the calorimeters. Due to the origin of the projection at the beam interaction point, the radial coordinates of these boundaries, projected to the reference layer 7, have a small relative shift between adjacent layers of about 200 μm at the inner radius and about 350 μm at the outer radius. The arrows mark the position of a given pad boundary in layer $7\,{\rm X}_0$, deeper layers have a lower R and shallower layers a higher R. Note that in contrast to the acceptance bands also shown in this figure, these anchoring points are independent of the Monte Carlo, and do not depend on the assumed running of α.

While the braod features of the acceptance bands are sensitive to the running assumed in the Monte Carlo, the small scale, local structure in the bands reveals even very small residual imperfections in the reconstructed coordinate. The essential point of Fig. 6 is that where the anchor points derived from individual pad boundaries follow these local variations in the relative acceptance band the radial bias determined by the anchoring procedure is seen to be consistent with this residual structure in the coordinate. In contrast, wherever the anchor points exhibit a local pattern of divergence from the acceptance band, especially as a function of depth, this indicates an anomaly in these anchors. Most anchors are found to be consistent

with the relative acceptance band. However, clear discrepancies are apparent for the deepest layers considered (8-10 X_0), in particular for the Left side. This is most evident in the central region of acceptance, where the amount of material between the detector and the interaction point is large and the parameterization of the expected bias derived from the test beam is evidently no longer applicable. The behaviour of the anchors with depth indicates that the onset of these problems is abrupt, and a large region of the detector remains well understood for use in our analysis. Notice that in the obscured region of the detector the run-away of the anchors occurs almost exactly one layer earlier on the Left side of the detector, at layer $8\,X_0$, than it does on the Right, indicating that the $0.5\,X_0$ of additional preshowering material has an effect larger than an equivalent amount of compact absorbing material within the detector.

The plotted relative acceptance band depends on the running of α that we want to measure, so its remarkably flat shape means that the data agrees with the input $\alpha(t)$ in the Monte Carlo. To make this clear we have also plotted the prediction for zero running as the hatched bands. The highly significant "eyebrow" shape of the zero-running acceptance bands and their clear separation from the flat Standard Model bands is a graphic representation of the sensitivity of our measurement.

The run-away anchors in the deepest layers considered are consistent with the eyebrows, however, and show that the effects of the preshowering material for these deep layers, particularly on the Left side, would give an apparent shape consistent with zero running. As mentioned previously this is equivalent to biases of about $70\,\mu$m in the middle of the acceptance.

6 Finding safe anchors for the measurement

In order to see more directly the effect of anchoring imperfections on the fitted slope b, we have made a series of test fits for each choice of anchoring layer. The fits are simple χ^2 fits of the ratio of data to Monte Carlo events observed in each bin to the two coefficients of Equation (7). The Monte Carlo in this case assumes a constant coupling $\alpha(t) \equiv \alpha_0$. Since anchoring problems may manifest themselves either as increased fluctuations from bin to bin, or as broader, more dangerous, systematic effects highly correlated between nearby bins, we pursue two lines of investigation.

In the first we divide the radial distribution into the maximum number of bins: at each layer a bin corresponds to one of the 24 pads in the fiducial region. Since the assessed systematic errors are somewhat correlated from bin to bin, we consider only statistical errors, which are in any case dominant. We focus on the difference in χ^2 between the anchored and unanchored distributions, which is shown in Fig. 7 as a function of the anchoring layer. The results are shown separately for the two sides, and for the two homogeneous data combinations, 1993-94 and 1995. It is apparent that beyond layer $7\,X_0$ the χ^2 becomes progressively worse. This agrees with the run-away of the anchors in deep layers which was shown in Fig. 6. In contrast, the anchoring procedure appears stable in layers 1-6 X_0.

Fig. 8 gives an illustration for the combination of all data, anchored at layer $4\,X_0$. The fit χ^2 is 41.3/22 for the Right side and 133.2/22 for the Left side after the anchoring correction. The fit quality is much worse for the Left side as is apparent from the greater dispersion of the points. The anchoring procedure improves the χ^2 for the Right side but not for the Left:

unanchored distributions have $\chi^2 = 47.9/22$ and $124.6/22$ respectively. Allowing for the known anchoring systematic errors, as explained in Section 7.1, a good χ^2 is obtained for the Right side distribution, while the χ^2 on the Left is still too large.

In the second study, we focus on broader systematic effects which have a direct impact on the measured running. Here we optimise the number of bins for extraction of the slope b, as specified in Table 1 (for layer $4\,X_0$). This binning is more consistent with the small number of parameters we wish to extract. The bin width grows with increasing radius to compensate the diminishing statistics, and any noise associated with fluctuations at the suppressed intermediate bin boundaries, which we tested in our first study, is reduced. Here, in addition to the statistical errors, we also include the systematic errors of the anchoring procedure, determined as described in Section 7.1. The fitted values of b for each layer are shown in Fig. 9. In each case the band shows the result obtained from the unanchored radial distribution, where the width corresponds to the statistical error. Unlike the anchored points, the unanchored results are independent of depth, and the small shifts only reflect binomial errors associated with the rebinning of the distribution in each layer. By applying the anchoring corrections the slope b does not change more than its statistical error in layers 1-6 X_0 and then shows a steady decrease with increasing depth in the calorimeters. Layer $0\,X_0$ shows a strong deviation from the unanchored result, in the opposite sense. For 1993-94 data the onset of deviations on the Left side precedes that on the Right by almost exactly one layer, consistent with Fig. 6, due to the presence of the extra preshowering material of the microvertex cables. In the 1995 data the observed deviations are similar on the two sides, reflecting the fact that the preshowering material is then symmetric.

The anchored slope is remarkably flat for the broad region covering layers 1-6 X_0 in the 1993-94 Right data. Here the individual results are consistent within the assigned systematic errors. For the other datasets the values of the anchored slope in layers 1-6 X_0 are distributed within twice the assigned systematic errors. Similarly the difference between the individual values of the anchored and unanchored slope is within twice the assigned systematic error in each case. The Left side appears to exhibit a pattern of deviations consistent with a residual depth-dependent effect, particularly in the more statistically significant 1993-94 data. Due to the back-to-back nature of Bhabha events, the two sides do not contribute independent statistical information. We therefore choose to derive our final results from the Right side alone. Even though in 1995 the Right data are affected by extra preshowering material to an extent similar to the 1993-94 Left data, we consider that the gain of statistical precision in using these independent data outweighs the risk of any potential increase in systematic error. Possible unaccounted systematic errors related to the preshowering material are estimated in section 7.2. We also choose the anchors in layer $4\,X_0$ to correct our final results, since this layer lies in the centre of the safe region, where the anchoring procedure is valid.

7 Systematic uncertainties

Having discussed how we ensure that our anchoring corrections are chosen from a safe region of the detector, we now quantify the residual errors we attribute to these anchors, as well as all other systematic errors we identify as affecting the measurement. The analysis of these errors closely follows their treatment in the SiW luminosity analysis [14]. The discussion here focuses on those considerations specific to the current measurement, and quantifies their effect, δb, on

the extracted value of b. The systematic uncertainties are grouped into classes and discussed in detail below.

7.1 Anchoring errors

This error class includes all the uncertainties connected with the anchoring procedure described in Section 5. Biases on the radial coordinate can directly affect the shape of the t distribution. In particular a bias on the reconstructed position in the central part of the acceptance, behind the preshowering material, can produce a significant error. As mentioned in Section 2, a bias in the central region of 70 μm would double the expected apparent running or reduce it to zero depending on the sign of the bias.

Shifts in the anchors can arise either through the measured value of $R_{\rm off}$ or through the determination of the pad boundary bias, $\delta R_{R\phi}$. The measurement of $R_{\rm off}$ is affected by pad gain fluctuations and departures from the Gaussian model used for fitting the pad boundary image. A global uncertainty in the pad boundary bias $\delta R_{R\phi}$ has negligible effect on the current measurement, but uncertainty in its radial dependence must be considered.

The observed $R_{\rm off}$ is affected by fluctuations in the individual pad gains. We have checked these effects directly on data, by studying $R_{\rm off}$ for each of the 32 azimuthal divisions of the calorimeters. The size of the extra azimuthal variations, after allowing for the statistical and the metrology fluctuations, is taken as the systematic uncertainty due to pad gain variations. We assign the statistically expected shift in the mean $(R_{\rm off})^{\rm extra}_{\rm RMS}/\sqrt{32}$ as a systematic error in the anchors. This is a genuine uncorrelated error as a function of radius, estimated to contribute $\delta b = 32(30) \times 10^{-5}$ for the 1993-94 (1995) data.

Another error component uncorrelated with radius is the statistical error of the anchors, determined from the fits of the pad boundary images. This gives a further $\delta b = 10(20) \times 10^{-5}$ for the 1993-94 (1995) data.

Fig. 3 shows that a Gaussian resolution does not perfectly describe the tails of the pad boundary image. To the extent that this image maintains an odd symmetry about the apparent pad boundary, its non-Gaussian behaviour does not affect the determination of $R_{\rm off}$, as can be seen from the close agreement of the data points and the fitted curve near the pad boundary. We have also considered a model in which the apparent pad boundary is taken as the median of the observed resolution function. The shift in the slope which is obtained with this alternative method is taken as an error. In the safe region of the detector it is very small, $\delta b = 2(12) \times 10^{-5}$ for 1993-94 (1995) data. In the deeper layers of the detector, however, this error source becomes significant, and may be underestimated. In fact we suspect that this effect may contribute to the observed run-away of the anchors at large depths.

The determination of the pad boundary bias in the test beam was carried out at a radial position close to the inner acceptance cut to provide optimal information for the luminosity determination. In this analysis we have a greater dependence on knowing the pad boundary bias throughout the detector. The geometrical bias due to R-ϕ pads is expected to scale as $1/R$, thus decreasing at a greater radius of pad curvature. Therefore we have scaled the bias estimated using the test beam results, but assign an additional systematic error equal to 50% of the expected bias to account for possible deviations from this behaviour. We have estimated

conservatively the effect of this additional error, by shifting in a correlated manner all the anchors by this error and taking the resulting variation in the slope. This is found to be $\delta b = 25(32) \times 10^{-5}$ for the 1993-94 (1995) data.

Further errors on the determination of $\delta R_{R\phi}$ have been estimated for the worst case of a bias anticorrelated between the inner and the outer radius. Under this conservative hypothesis, the uncertainty on the shower width dependence of the pad boundary bias may contribute a shift of $\delta b = 11 \times 10^{-5}$, common to all the datasets. The uncertainty on the input apparent width $\sigma_{\rm a}$ may shift the slope by $10(19) \times 10^{-5}$ for the 1993-94 (1995) data.

All these error contributions have been summed in quadrature, giving finally a total anchoring error on the slope b of $45(52) \times 10^{-5}$ for the 1993-94 (1995) data. This corresponds to an effective anchoring error of about 4 μm.

7.2 Preshowering material

To cover in a conservative way possible effects of the preshowering material we made a few direct tests using the data. The amount of preshowering material is maximum in the middle of the accepted radial range, as is reflected in the $\sigma_{\rm a}$ distribution shown in Fig. 5. We have thus defined two regions:

- *clean* region, $R \leq 8.2$ cm and $R \geq 11.7$ cm, corresponding to the first 4 pads starting from the inner radial cut and the last 6 pads close to the outer cut;
- *obscured* region, $8.2 < R < 11.7$ cm, corresponding to the central 14 pads.

The fitted slopes determined separately in the two regions and in the full acceptance are given in Table 2. We see that the results obtained in the clean region are quite close to the results of the fit over the full acceptance. Moreover the independent values obtained in the obscured region are consistent within the statistical errors. It is natural to expect a possible extra pad boundary bias in the obscured region, particularly on the Left side. We have checked for its presence by introducing a new parameter x in the fit, related to this assumed extra bias, using two alternative models:

- *Box-model*, a naive choice assuming a constant extra bias within the obscured region and no extra bias in the clean region. Here x is the constant extra bias.
- *W-model*, the extra bias $\delta R_{\rm extra}$ is assumed to follow the pattern of the apparent shower width $\sigma_{\rm a}$ versus R:

$$\delta R_{\rm extra} = x \frac{\sigma_{\rm a}(R) - \sigma_{\rm a}(R_{\rm min})}{\sigma_{\rm max} - \sigma_{\rm a}(R_{\rm min})} \tag{15}$$

  where $R_{\rm min}$ is the inner acceptance cut (where $\sigma_{\rm a}$ is minimum) and $\sigma_{\rm max}$ is the maximum value of $\sigma_{\rm a}$, which is reached near the centre of the detector ($R \approx 10.2$ cm). Therefore $\delta R_{\rm extra} = x$ when $\sigma_{\rm a}(R) = \sigma_{\rm max}$.

No evidence for an extra bias is found under either of the two hypotheses. We take the statistical sensitivity of the check as a systematic uncertainty, quantified as the additional contribution to the error on the slope generated by allowing the possibility that such an extra bias might exist. We obtain $30(53) \times 10^{-5}$ for the Right (Left) side in 1993-94 data and $87(94) \times 10^{-5}$ for the Right (Left) side in 1995 data. Notice that such uncertainties cover the observed shifts between fits in the restricted clean region and in the full acceptance in each of the various cases.

7.3 Position resolution

The radial resolution at pad boundaries in the clean acceptance near the inner edge of the detector has been measured using the test beam to be 130 μm. The apparent resolution at the outer edge and in the central portion of the detector, behind the bulk of the preshowering material, is degraded by a factor of 2 to 2.5, according to the pattern of Fig. 5. The Monte Carlo simulation includes a radial dependence accounting for this variation. The impact of any unaccounted degradation of the radial resolution as a function of radius is tiny. For example, to get an effect the same size as the running, the resolution behind the material would have to be wrong by 2 mm. We conservatively assessed the uncertainty related to the radial resolution by dividing the acceptance into two radial bins and calculating the full effect of the resolution flow on the slope. It amounts to $15(25) \times 10^{-5}$ for 1993-94 (1995) data. The contribution of the resolution flow across the acollinearity cuts is negligible in comparison, amounting to less than 5×10^{-5} in all cases.

The resolution of the reconstructed azimuthal coordinate is not critical because of the cylindrical symmetry of the detector. It only enters through the cuts on the acoplanarity distribution as a resolution flow effect, which is taken into account by the detector simulation. Radial variation of the azimuthal resolution and unaccounted non-Gaussian tails give uncertainties on the slope smaller than 3×10^{-5} and have been neglected.

7.4 Acollinearity bias

In contrast to the radial distribution, the acollinearity distribution, with the selection cut $|\Delta R| \leq 2.5$ cm, is not corrected for radial biases. It is therefore subject to biases of the order of the anchors themselves. In the worst case there could be a first order effect causing a net gain or loss of events at both the positive and the negative ΔR cut. This is conservatively estimated by considering a bias with absolute value $\Delta R_{\rm bias} = 30$ μm, which is the maximum reached by the anchors. This corresponds to an uncertainty on the slope of 9×10^{-5}.

7.5 Metrology

The detector geometry was carefully determined and monitored for the luminosity measurement [14]. The most crucial quantity in that analysis was the inner radius of the calorimeters, since the internal geometry of the Si wafers is inherently excellent. This analysis is much less sensitive to the absolute radial scale, and it would require a radial shift of about 0.5 mm to mimic the

expected α running. Even without averaging over the measurements of the two sides, the inner radii are known with a precision of 7 μm, which gives an error on the slope of only 12×10^{-5}.

In operating conditions thermal effects also contributed variations to the nominal radial dimensions of the detector on the order of 2-10 μm. These were calculated independently for each data set, according to the average temperature measured by thermistors located on each detector layer. Such thermal effects give contributions to the slope of 3-13 $\times 10^{-5}$, which have been considered correlated between all the data samples.

This analysis is insensitive to longitudinal metrology errors. In fact an error in the longitudinal separation between the Right and Left calorimeters would be equivalent to a shift in the z position of the interaction vertex which has no effect on the slope. Also the inter-layer separation gives negligible uncertainties: for a change of 100 μm in the spacing between layers, the effect on the slope is about 1×10^{-5} for all layers considered (1-10 X_0).

7.6 Beam parameters

The geometry of the colliding beams with respect to the detector can have quite important effects on the apparent slope. The expected α running has an effect comparable to an uncorrected transverse offset of the beams of 4 mm or a beam angular divergence of 1.4 mrad. These values are much larger than those we experienced. Moreover we were able to determine such parameters from the data.

Variations in the beam parameters modify the geometric acceptance of the definition cuts in a manner which can be adequately calculated analytically by assuming a simple $1/\theta^3$ angular distribution. The effect of the isolation cuts is less tractable analytically, but since they considerably decrease the variations calculated from the acceptance cuts alone, their neglect yields a conservative estimate of the uncertainties. The effects on the slope b may be estimated with sufficient precision by dividing the radial acceptance into two bins.

The definition cuts are sensitive only to the sum of the transverse beam offset and the beam tilt. The transverse beam offset is measured run-by-run with a precision better than 10 μm and gives a negligible uncertainty on the fitted slope. The beam tilt is therefore the most important effect. Its two components are determined run-by-run as the difference of the eccentricities of the unscattered beams as they pass through the bore of each calorimeter. These eccentricities are measured by the azimuthal modulation of the Bhabha intensity, and the statistical accuracy with which they can be determined is 200-300 μm for typical runs. For the nine data sets the beam tilt contributes 2-9 $\times 10^{-5}$ to the uncertainty in the slope. These errors have been conservatively taken twice: both correlated and uncorrelated. Although they are unlikely, we have no way of measuring rapid tilt variations, on a time scale shorter than an individual run, we have therefore taken as an additional uncertainty the slope variation corresponding to the extreme hypothesis of setting the beam tilt to zero. This uncertainty ranges from 2×10^{-5} for the largest sample (94-b) to 32×10^{-5} in the worst case. We have taken such numbers as uncorrelated errors, with an additional common correlated systematic error equal to 2×10^{-5}.

The transverse beam size and divergence give effects similar to the radial resolution and can be estimated, in an analogous way, from the related resolution flow. The full effect of the beam size on the slope is about 1×10^{-5}, and has been neglected. The uncertainty on the

beam divergence, estimated by comparing two independent determinations, is about 100 μrad for 1993-94 data and about 130 μrad for 1995 data. The resulting uncertainties on the slope are 4×10^{-5} and 7×10^{-5} respectively. These errors have been conservatively taken twice: both correlated and uncorrelated.

The longitudinal position of the beam spot has a constant effect on the radial acceptance so gives no contribution to the slope. The same holds for the longitudinal size of the beam spot.

The uncertainties estimated analytically have been checked with the results of Monte Carlo simulations where one parameter at a time can be varied. In this manner the isolation cuts are included, at the price of some statistical limitation. The results are consistent.

7.7 Energy response

The essential problem here is how the preshowering material degrades the energy response and causes events to be lost from the accepted sample. Uncertainties due to the energy response have been assessed by varying the parameters in the detector simulation within the precision to which they have been estimated from the data. They include the Gaussian width of the energy response function, the exponential low-energy tail, the nonlinearity and the method used to extrapolate the energy resolution to lower energies. We determined the variation in the fitted slope in a conservative way, by dividing the radial acceptance into two bins and then by changing in turn each parameter in the simulation of the outer bin, leaving unchanged the parameters for the inner bin. Then we took the sum in quadrature of all the variations. The dominant uncertainty is caused by the low-energy tail of the response function, which is generated by events that shower very late in the detector, events not fully contained and events with electrons and positrons that scatter in upstream material. The resulting uncertainty is 27×10^{-5}.

7.8 Accidental background

Off-momentum electrons and positrons generated by beam-gas scattering generate the majority of single showers observed in the luminometer. Accidental coincidences between background clusters in the Right and Left calorimeters can occasionally produce events which are selected as Bhabha scatterings, although in general these events are rejected by the minimum energy cuts or fail the acollinearity cuts. This background was studied by special triggers including random bunch crossings and delayed coincidences. The background fractions were found to vary between 0.1 and 0.6×10^{-4} depending on the data set [14]. We have estimated the effect on the slope by dividing the acceptance into two radial bins and assuming that the background is concentrated in the inner bin. The radial distribution of background is indeed sharply peaked at low radius. To account for the enlarged acceptance used in this analysis we increased the background fractions by 50%, which covers the variations observed by studies of the background distributions. The effect on the slope is a slight decrease of between 2 and 16×10^{-5}, for which no correction has been applied. The full effect is taken as an uncertainty correlated between the data samples.

The accidental overlap of a background cluster with a Bhabha event can also change the values

of reconstructed quantities, modifying the acceptance. This has been evaluated by incorporating the measured background into the detector simulation, by adding to BHLUMI events background clusters with rates determined from random triggers. Likewise we have also combined the measured background with data. In both cases the resulting shift in the slope is smaller than 10^{-5} and has been neglected.

7.9 Physics biases in the fitted slope

The fit method used to determine the slope b has been studied on Monte Carlo samples. The logarithmic t dependence expressed by Equation (7) is followed very well. Actually in data we have no statistical sensitivity to the difference between a logarithmic and a simple linear behaviour. However, the parameterization in Equation (7) has the advantage that the logarithmic slope b is almost constant for small variations of the t range or the different centre-of-mass energies which we have in data. The fit method has a small bias at off-peak energies, due to effects of Z interference, of about $\delta b = \pm 14 \times 10^{-5}$, where the plus sign applies to energies above the peak energy and the minus sign below. This bias has been corrected on each data subsample, with negligible uncertainty. The final average would not suffer in any case from this small effect, which cancels when averaged over the roughly equal samples above and below the peak.

The reconstructed t has a small positive bias, due to initial-state radiation, with respect to the exchanged four-momentum between the electron and positron line. From a study of BHLUMI Monte Carlo events this bias is found to be almost zero at the inner acceptance cut, increasing to about 0.1 GeV^2 at the outer cut. This small variation of the t range has a negligible effect on the slope b.

Our selection contains a small irreducible physics background from the process $e^+e^- \to \gamma\gamma$, for which we apply a correction. Its cross section within our idealized acceptance is found to be 16.9 pb at 91.1 GeV using a Monte Carlo generator including $O(\alpha^3)$ terms [21]. The correction to the slope b is -18×10^{-5}, practically constant with respect to our range of centre-of-mass energies, with negligible uncertainty.

7.10 Summary of systematic errors

The dominant systematic errors are those related to anchoring and preshowering material, described in Sections 7.1 and 7.2.

The experimental systematic uncertainties are summarized in Table 3, where the nine data samples are labelled as in [14]. The final experimental error correlation matrix (including the statistical errors) is given in Table 4. The correlations reach at most 10%. The classification of the detailed sources of error into correlated and uncorrelated components given in Table 3 does not reveal the complete pattern of correlations embodied in the full correlation matrix. In that table the errors classified as correlated are fully correlated between all data samples, while some classified as uncorrelated are actually correlated within a given year, but uncorrelated between years.

8 Theoretical uncertainties

It is important to assess the theoretical uncertainties associated with our reference cross section calculated by the BHLUMI Monte Carlo. In fact a reliable determination of the running coupling constant from Equation (2) needs a precise knowledge of the radiative corrections.

The BHLUMI Monte Carlo is a multiphoton exponentiated generator for small-angle Bhabha scattering. Its matrix element includes complete $\mathcal{O}(\alpha)$ and $\mathcal{O}(\alpha^2 L^2)$ photonic corrections. Higher order contributions are partially included by virtue of the exponentiation. The theoretical uncertainty in the BHLUMI calculation has been studied extensively for the event selections of the LEP experiments. The fractional theoretical error is 6.1×10^{-4} for the integrated cross section at LEP 1 [16, 22] which was relevant for the determination of the luminosity. Alternative existing calculations have been widely cross-checked with BHLUMI [16]. Moreover the extensive comparisons between data and the predictions of the Monte Carlo by the four LEP collaborations decrease the chances that it contains significant residual technical imperfections.

We also use two other Monte Carlo generators which are included in the same BHLUMI package. OLDBIS [23, 24] is an exact $\mathcal{O}(\alpha)$ calculation, based on a Monte Carlo program written by an independent group. LUMLOG [18, 25] implements a Leading-Log calculation up to $\mathcal{O}(\alpha^3 L^3)$, based on a structure function approach, assuming purely collinear radiation. The BHLUMI package gives access to many intermediate weights which compose the final calculations, so that we have also checked several different approximations.

For the purpose of assessing the theoretical uncertainties, the OPAL experimental selection has been described by a slightly modified version of the code used in [16] and included in the BHLUMI package (subroutine `TRIOSIW`). Events have been generated within a safely enlarged angular region to protect against loss of visible events. Smearing effects are neglected and an ideal beam geometry is assumed. Nearby particles are combined by a clustering algorithm which has a window matched to the experimental resolution. The energy is defined by summing all the particles inside the isolation cuts in each calorimeter. The position variables R and ϕ are defined as the coordinates of the highest energy particle reconstructed on each side. We have applied all the isolation cuts listed in Section 4 to these reconstructed variables. The size of the window used by the clustering algorithm (in R and ϕ) has been varied over a large range to verify the stability of the result. As further checks we have used alternative selections, for example SICAL (following the nomenclature of [16]) which mostly differs in its lack of acollinearity cuts, and BARE, a non-calorimetric selection.

The differential cross section obtained at different perturbative orders is shown in Fig. 10 normalized to the reference BHLUMI cross section. Here vacuum polarization, Z-exchange interference and s-channel photon interference have been switched off. Radiative corrections reduce the Born cross section by about 5-15%, depending on the polar angle. Most of the reduction is obtained by the leading $\mathcal{O}(\alpha L)$ corrections, which give a result uniformly about 1% above the reference. When the complete $\mathcal{O}(\alpha)$ corrections are considered, including subleading terms, the result lies below, generally within 1% of the reference but with stronger edge effects. The most precise alternative calculation shown in Fig. 10 is the sum of the complete $\mathcal{O}(\alpha)$ given by OLDBIS and the leading higher orders ($\mathcal{O}(\alpha^2 L^2)$ and $\mathcal{O}(\alpha^3 L^3)$) given by LUMLOG. This combination was previously used in [16], and is termed OLDBIS+LUMLOG in what follows.

Examination of the canonical coefficients [26] indicates that for a calorimetric detector accep-

tance such as ours the $\mathcal{O}(\alpha^2 L)$ and $\mathcal{O}(\alpha^3 L^3)$ terms dominate the approximately calculated portion of the complete BHLUMI cross section.

The effect of $\mathcal{O}(\alpha^3 L^3)$ terms on the slope b measured within our selection can be directly calculated using LUMLOG and is found to be small, $(-10 \pm 9) \times 10^{-5}$. Moreover such terms are known to be almost completely accounted for by the exponentiation in BHLUMI.

The magnitude of the $\mathcal{O}(\alpha^2 L)$ corrections can be roughly estimated from the product of the leading $\mathcal{O}(\alpha L)$ and the subleading $\mathcal{O}(\alpha)$ corrections. This is about 0.5×10^{-3} times the Born cross section when integrated over the entire acceptance. The effect on the slope b is estimated by calculating this product for the inner and outer halves of the acceptance separately and then taking the difference. In this way we obtain $\delta b = 20 \times 10^{-5}$, which is expected to be correct within a factor of about 2.

A better test of the $\mathcal{O}(\alpha^2 L)$ corrections, which also takes into account the limited technical precision of the Monte Carlos, can be obtained by comparing the reference $\mathcal{O}(\alpha^2 L^2)$ exponentiated calculation of BHLUMI to the combination of the two independent Monte Carlos, OLDBIS and LUMLOG. The OLDBIS+LUMLOG combination is shown together with other precise calculations at our disposal in Fig. 11. To quantify possible deviations from the expected t shape, we fit the ratios of alternative calculations to the reference BHLUMI with a linear t dependence. The effect, δb, on our measured slope b is then estimated by accounting for the factor $|t_2 - t_1|/\ln(t_2/t_1) = 3.52$ which converts from a linear to a logarithmic t range. We obtain:

$$\begin{aligned} \delta b\,[(\text{OLDBIS} + \text{LUMLOG})/\text{BHLUMI}] &= (-38 \pm 20) \times 10^{-5} \\ \delta b\,[\text{Exp.}\mathcal{O}(\alpha)/\text{BHLUMI}] &= (+22 \pm 16) \times 10^{-5} \\ \delta b\,[\text{Unexp.}\mathcal{O}(\alpha^2 L^2)/\text{BHLUMI}] &= (-11 \pm 61) \times 10^{-5}\,. \end{aligned}$$

The ratio of the exponentiated $\mathcal{O}(\alpha)$ calculation to the full BHLUMI is quite flat as a function of t, with a clear normalization shift of 0.2%, which is however irrelevant to our analysis. The unexponentiated $\mathcal{O}(\alpha^2 L^2)$ also seems flat, albeit with much larger statistical error bars. The OLDBIS+LUMLOG combination is rather flat with somewhat larger than expected fluctuations. The extreme points on either end show downward deviations with respect to the reference BHLUMI, but removing them does not change the fit significantly. We take the shift δb determined from the (OLDBIS + LUMLOG)/BHLUMI fit as the uncertainty due to missing higher orders, which are mainly $\mathcal{O}(\alpha^2 L)$, plus the technical precision of the calculations. This amounts to 38×10^{-5}, which is in agreement with our cruder estimate obtained from the product of the leading $\mathcal{O}(\alpha L)$ and the subleading $\mathcal{O}(\alpha)$ terms, above. This estimate is also seen to be in line with the differences observed for the exponentiated $\mathcal{O}(\alpha)$ and the unexponentiated $\mathcal{O}(\alpha^2 L^2)$ calculations. Changing the size of the window used by the clustering algorithm produces negligible variations. Similar results are also obtained for the SICAL selection.

The interference with the Z-exchange amplitude in the s-channel is a small correction, designated δ_{Z} in Equation (2), which is not factorized with respect to the main contribution and the running coupling constant. It is energy dependent, vanishing at $\sqrt{s} = m_{\text{Z}}$ and changing sign across the Z pole. In BHLUMI it is calculated up to exact $\mathcal{O}(\alpha)$ photonic corrections, which can also be exponentiated [27]. Vacuum polarization can be included. Event samples have been generated at three different energies: the Z-peak energy ($\sqrt{s} = 91.1$ GeV) and energies offset by ± 2 GeV. At each energy we consider independently the shifts in the slope b produced

by switching off the exponentiation or the vacuum polarization for the calculated interference term δ_Z, and then add these shifts in quadrature. The maximum value of 30×10^{-5}, which is obtained at the peak, is taken as the uncertainty due to Z interference.

Concerning the contribution of the vacuum polarization to the δ_Z term, this subtle effect could in principle perturb the asserted cleanliness of the measurement. However such an effect is vanishingly small at the peak energy ($\delta b = -6 \times 10^{-5}$ at $\sqrt{s} = 91.1$ GeV) and has approximately equal and opposite values smaller than $\pm 20 \times 10^{-5}$ above and below the pole. The overall effect is therefore negligible.

BHLUMI does not include diagrams with extra light lepton pairs (e^+e^-, $\mu^+\mu^-$). Their contribution was calculated explicitly for the OPAL selection, giving a fractional correction of $(-4.4 \pm 1.4) \times 10^{-4}$ [28] on the integrated cross section. The leading order contribution can be checked with LUMLOG, and gives effects on the slope b below 11×10^{-5} with the OPAL or the SICAL data selections.

The estimated theoretical uncertainties are summarized in Table 5. Their quadratic sum is 50×10^{-5} and will be added to the experimental errors.

9 Results

The final results are based on the radial distribution observed in the Right side calorimeter, corrected by the anchoring procedure, as explained in Sections 5-6. The correction employs the anchors determined in layer $4\,X_0$, which is in the middle of the safe region. Within this region the anchored and unanchored results have been shown to be in fairly good agreement. The decision to use only the Right calorimeter and to use anchored coordinates, as well as the choice of the anchoring layer, are aimed to achieve our best experimental accuracy and to minimize possible unassessed systematic errors. Consistent results, within the quoted final systematic error, are in fact obtained if any of these choices are changed.

The radial distribution is binned as specified in Table 1. The numbers of data and Monte Carlo events in each bin for the largest subsample (94b) are reported in Table 6. Note that here the Monte Carlo assumes $\alpha(t) \equiv \alpha_0$. The bin-by-bin acceptance corrections, obtained from Equations (11) and (12) by inserting the estimated radial biases at the relevant bin boundaries, are also given.

The ratio of data to Monte Carlo is fitted with the logarithmic t-dependence of Equation (7) separately for each dataset and the results are reported in Table 7. Both the dominant statistical errors and the experimental systematic errors, which are determined as described in Section 7, are shown. The small corrections for the irreducible background and Z interference have been applied to the quoted b values. The nine subsamples (labelled as in [14]) give consistent results, with $\chi^2/\text{d.o.f} = 6.9/8$ for the average b considering only statistical errors. We have checked for a possible residual energy dependence of the measured slope b, which might be observed if the calculated Z interference contribution disagreed with the data. Within the statistical errors of the data we find no such energy dependence.

We combine the results of the nine subsamples using the error correlation matrix in Table 4,

obtaining:

$$b = (726 \pm 96 \pm 70 \pm 50) \times 10^{-5}$$

where here, and also in the results quoted below, the first error is statistical, the second is the experimental systematic and the third is the theoretical uncertainty, discussed in section 8. The total significance of the measurement compared to the hypothesis of $b = 0$ is $5.6\,\sigma$.

The result for the combined data sample is illustrated in Fig. 12. The error bars shown are statistical only, since many of the systematic errors are estimated only for the fitted slope in the individual subsamples and not bin-by-bin. The logarithmic fit to Equation (7) describes the data very well, $\chi^2/\text{d.o.f} = 1.9/3$, although a simple linear fit would also be adequate, giving $\chi^2/\text{d.o.f} = 2.7/3$. The data are clearly incompatible with the hypothesis of a fixed coupling. The fitted logarithmic dependence agrees well with the full Standard Model prediction including both leptonic and hadronic contributions, with the hadronic part obtained by the Burkhardt-Pietrzyk parameterization [3]. Older parameterizations of the hadronic component, like [2] or [19], would be indistinguishable from the curve shown. Our result is consistent with the similar measurement by L3 [13]. If the latter is expressed as a slope according to (8), it gives $b^{(L3)} = (1044 \pm 348) \times 10^{-5}$, where the error is dominated by experimental systematics.

Our measurement of the effective slope gives the variation of the coupling $\alpha(t)$ from Equation (8):

$$\Delta\alpha(-6.07\,\text{GeV}^2) - \Delta\alpha(-1.81\,\text{GeV}^2) = (440 \pm 58 \pm 43 \pm 30) \times 10^{-5}\,.$$

This is currently the most significant direct observation of the increase of the effective QED coupling strength with increasing momentum transfer. The result is in good agreement with the Standard Model prediction, which gives $\delta\,(\Delta\alpha) = (460 \pm 8) \times 10^{-5}$ for the same t interval. Here the error has been calculated by assuming the uncertainties on $\Delta\alpha_{had}$ at $t = -1.81\,\text{GeV}^2$ and $t = -6.07\,\text{GeV}^2$ (of 2.5 % and 2.7 % respectively [29]), which arise from the hadronic component, are fully correlated. If the errors on $\Delta\alpha_{had}$ at the extreme values of t are assumed to be uncorrelated, the error would increase to 23×10^{-5}.

The absolute value of $\Delta\alpha$ in our range of t is expected to be dominated by e^+e^- pairs, with the relevant fermion species contributing in the approximate proportions: $e : \mu : \text{hadron} \simeq 4 : 1 : 2$. Our measurement is sensitive, however, not to the absolute value of $\Delta\alpha$, but only to its slope within our t range. Contributions to the slope b in this range are predicted to be in the proportion: $e : \mu : \text{hadron} \simeq 1 : 1 : 2.5$. Fig. 12 shows these expectations graphically. We can discard the hypothesis of running due only to virtual e^+e^- pairs with a significance of $4.4\,\sigma$.

The data are also incompatible with the hypothesis of running due only to leptons. If we subtract the precisely calculable theoretical prediction for all leptonic contributions, $\delta(\Delta\alpha_{\text{lep}}) = 202 \times 10^{-5}$, from the measured result, we can determine the hadronic contribution as:

$$\Delta\alpha_{\text{had}}(-6.07\,\text{GeV}^2) - \Delta\alpha_{\text{had}}(-1.81\,\text{GeV}^2) = (237 \pm 58 \pm 43 \pm 30) \times 10^{-5}\,.$$

This differs from zero by $3.0\,\sigma$, considering all the errors. In comparison to other existing direct measurements of the QED coupling, our result has sufficient sensitivity to expose clearly the hadronic contribution to the observed variation of α as a function of the momentum transfer.

10 Conclusions

We have measured the scale dependence of the effective QED coupling $\alpha(t)$ from the angular distribution of small-angle Bhabha scattering using the precise OPAL Silicon-Tungsten calorimeters. Despite the narrow accessible t range, the method has high sensitivity due to the large statistics and excellent purity of the data sample. The challenging aspect of the analysis is controlling the residual bias in the reconstructed radial coordinate of Bhabha electrons in the detector to a level below $\approx 10\,\mu$m uniformly throughout the acceptance. From a theoretical point of view the measurement is almost ideal. For this kinematic range the process is almost purely QED, Z interference is very small and the dominant diagram is t-channel single-photon exchange, while s-channel photon exchange is negligible. Due to its utility in determining the LEP luminosity, small-angle Bhabha scattering is one of the most precisely calculated processes at these energies. We verified that there is no significant disturbance from theoretical uncertainties.

We determined the effective slope of the Bhabha momentum transfer distribution which is simply related to the average derivative of $\Delta\alpha$ as a function of $\ln t$ in the range $2\ \mathrm{GeV}^2 \leq -t \leq 6\ \mathrm{GeV}^2$. The observed t-spectrum is in good agreement with Standard Model predictions. We find:

$$\Delta\alpha(-6.07\,\mathrm{GeV}^2) - \Delta\alpha(-1.81\,\mathrm{GeV}^2) = (440 \pm 58 \pm 43 \pm 30) \times 10^{-5}\,,$$

where the first error is statistical, the second is the experimental systematic and the third is the theoretical uncertainty.

This measurement is one of only a very few experimental tests of the running of $\alpha(t)$ in the space-like region, where $\Delta\alpha$ has a smooth behaviour. We obtain the strongest direct evidence for the running of the QED coupling ever achieved in a single experiment, with a significance above $5\,\sigma$. Moreover we report a clear experimental evidence for the hadronic contribution to the running in the space-like region, with a significance of $3\,\sigma$.

Acknowledgements

We thank M. Caffo and L. Trentadue for useful discussions. We particularly wish to thank the SL Division for the efficient operation of the LEP accelerator at all energies and for their close cooperation with our experimental group. In addition to the support staff at our own institutions we are pleased to acknowledge the
Department of Energy, USA,
National Science Foundation, USA,
Particle Physics and Astronomy Research Council, UK,
Natural Sciences and Engineering Research Council, Canada,
Israel Science Foundation, administered by the Israel Academy of Science and Humanities,
Benoziyo Center for High Energy Physics,
Japanese Ministry of Education, Culture, Sports, Science and Technology (MEXT) and a grant under the MEXT International Science Research Program,
Japanese Society for the Promotion of Science (JSPS),
German Israeli Bi-national Science Foundation (GIF),

Bundesministerium für Bildung und Forschung, Germany,
National Research Council of Canada,
Hungarian Foundation for Scientific Research, OTKA T-038240, and T-042864,
The NWO/NATO Fund for Scientific Research, the Netherlands.

References

[1] P. J. Mohr and B. N. Taylor, Rev. Mod. Phys. **72** (2000) 351.

[2] S. Eidelman and F. Jegerlehner, Z. Phys. C **67** (1995) 585.

[3] H. Burkhardt and B. Pietrzyk, Phys. Lett. B **513** (2001) 46.

[4] The LEP Collaborations ALEPH, DELPHI, L3 and OPAL, the LEP Electroweak Working Group, the SLD Electroweak and Heavy Flavour Groups, CERN-PH-EP/2004-069, hep-ex/0412015.

[5] J. F. de Troconiz and F. J. Yndurain, Phys. Rev. D **71** (2005) 073008.

[6] S. L. Adler, Phys. Rev. D **10** (1974) 3714.

[7] S. Eidelman, F. Jegerlehner, A.L. Kataev, O. Veretin, Phys. Lett. B **454** (1999) 369; F. Jegerlehner, hep-ph/0308117.

[8] J. Bailey *et al.*, Nucl. Phys. B **150** (1979) 1.

[9] D. W. Hertzog and W. M. Morse, Ann. Rev. Nucl. Part. Sci. **54** (2004) 141.

[10] TOPAZ Collaboration, I. Levine *et al.*, Phys. Rev. Lett. **78** (1997) 424.

[11] OPAL Collaboration, G. Abbiendi *et al.*, Eur. Phys. J. C **33** (2004) 173.

[12] VENUS Collaboration, S. Odaka *et al.*, Phys. Rev. Lett. **81** (1998) 2428.

[13] L3 Collaboration, M. Acciarri *et al.*, Phys. Lett. B **476** (2000) 40.

[14] OPAL Collaboration, G. Abbiendi *et al.*, Eur. Phys. J. C **14** (2000) 373.

[15] A. B. Arbuzov, D. Haidt, C. Matteuzzi, M. Paganoni and L. Trentadue, Eur. Phys. J. C **34** (2004) 267.

[16] S. Jadach, O. Nicrosini *et al.*, in *Physics at LEP 2*, CERN 96-01, ed. G. Altarelli, T. Sjöstrand and F. Zwirner (CERN, Geneva, 1996), Vol. 2, pages 229–298.

[17] A.B. Arbuzov, V.S. Fadin, E.A. Kuraev, L.N. Lipatov, N.P. Merenkov and L. Trentadue, Nucl. Phys. **B485** (1997) 457.

[18] S. Jadach, W. Płaczek, E. Richter-Wąs, B. F. L. Ward and Z. Wąs, Comput. Phys. Commun. **102** (1997) 229.

[19] H. Burkhardt and B. Pietrzyk, Phys. Lett. B **356** (1995) 398.

[20] OPAL Collaboration, K. Ahmet *et al.*, Nucl. Instrum. Meth. A **305** (1991) 275.

[21] F. A. Berends and R. Kleiss, Nucl. Phys. B **186** (1981) 22.

[22] B. F. L. Ward, S. Jadach, M. Melles and S. A. Yost, Phys. Lett. B **450** (1999) 262.

[23] F. A. Berends and R. Kleiss, Nucl. Phys. B **228** (1983) 537.

[24] S. Jadach, E. Richter-Wąs, B. F. L. Ward and Z. Wąs, Phys. Lett. B **253** (1991) 469; Comput. Phys. Commun. **70** (1992) 305.

[25] S. Jadach, E. Richter-Wąs, B. F. L. Ward and Z. Wąs, Phys. Lett. B **260** (1991) 438.

[26] G. Montagna, O. Nicrosini and F. Piccinini, Riv. Nuovo Cim. **21N9** (1998) 1.

[27] S. Jadach, W. Płaczek and B. F. L. Ward, Phys. Lett. B **353** (1995) 349.

[28] G. Montagna, M. Moretti, O. Nicrosini, A. Pallavicini and F. Piccinini, Phys. Lett. B **459** (1999) 649; Nucl. Phys. B **547** (1999) 39.

[29] H. Burkhardt and B. Pietrzyk, private communication.

Bin	$R_{\rm in}$	$R_{\rm out}$	$-t_{\rm in}$	$-t_{\rm out}$	$< -t >$
	(cm)		($\rm GeV^2$)		
1	7.2584	8.2665	1.81	2.35	2.05
2	8.2665	9.2746	2.35	2.95	2.63
3	9.2746	10.7868	2.95	3.99	3.42
4	10.7868	11.7949	3.99	4.77	4.36
5	11.7949	13.3071	4.77	6.07	5.37

Table 1: Bin definitions for the radial distribution. The corresponding $-t$ values are determined assuming a reference energy $\sqrt{s} = 91.2208$ GeV.

Detector side - Radial range	1993-94	1995	All
Right - full acceptance	757 ± 109	470 ± 198	690 ± 95
Right - clean	739 ± 129	566 ± 236	699 ± 113
Right - obscured	778 ± 239	247 ± 436	655 ± 210
Left - full acceptance	685 ± 108	417 ± 198	623 ± 95
Left - clean	680 ± 129	417 ± 236	620 ± 113
Left - obscured	766 ± 239	414 ± 437	685 ± 210

Table 2: Fitted slope for the full, clean and obscured radial range of acceptance in units of 10^{-5}, for homogeneous data subsamples and all data. Both the Right and the Left side results are given. The errors are statistical only.

Uncertainty	93 −2	93 pk	93 +2	94 a	94 b	94 c	95 −2	95 pk	95 +2
M.C. Statistics									
uncorrelated	56.	56.	56.	56.	28.	103.	56.	56.	56.
correlated	0.	0.	0.	0.	0.	0.	0.	0.	0.
Anchoring									
uncorrelated	10.	10.	10.	10.	10.	10.	29.	29.	29.
correlated	44.	44.	44.	44.	44.	44.	44.	44.	44.
Preshowering Material									
uncorrelated	0.	0.	0.	0.	0.	0.	81.	81.	81.
correlated	30.	30.	30.	30.	30.	30.	30.	30.	30.
Radial Resolution									
uncorrelated	0.	0.	0.	0.	0.	0.	0.	0.	0.
correlated	15.	15.	15.	15.	15.	15.	25.	25.	25.
Acollinearity Bias									
uncorrelated	0.	0.	0.	0.	0.	0.	0.	0.	0.
correlated	9.	9.	9.	9.	9.	9.	9.	9.	9.
Radial Metrology									
uncorrelated	0.	0.	0.	0.	0.	0.	0.	0.	0.
correlated	12.	12.	12.	12.	12.	12.	12.	12.	12.
Radial Thermal									
uncorrelated	0.	0.	0.	0.	0.	0.	0.	0.	0.
correlated	3.	3.	3.	4.	4.	4.	12.	12.	12.
Beam Parameters									
uncorrelated	19.	31.	20.	8.	5.	12.	12.	25.	33.
correlated	7.	7.	7.	7.	5.	9.	8.	8.	8.
Energy									
uncorrelated	0.	0.	0.	0.	0.	0.	0.	0.	0.
correlated	27.	27.	27.	27.	27.	27.	27.	27.	27.
Background									
uncorrelated	0.	0.	0.	0.	0.	0.	0.	0.	0.
correlated	16.	12.	7.	4.	2.	5.	4.	2.	2.
Sum									
uncorrelated	60.	65.	61.	58.	30.	104.	104.	106.	108.
correlated	66.	65.	64.	64.	64.	65.	68.	68.	68.
Total Systematic Error	89.	92.	89.	86.	71.	122.	124.	126.	128.

Table 3: Summary of the experimental systematic uncertainties on the measurement of the effective slope b for the nine data sets on the Right side. They are broken down into the components correlated and uncorrelated among the data sets. All errors are in units of 10^{-5}.

Sample	93 −2	93 pk	93 +2	94 a	94 b	94 c	95 −2	95 pk	95 +2
93 −2	1.00	0.04	0.04	0.04	0.07	0.02	0.04	0.03	0.04
93 pk	0.04	1.00	0.04	0.04	0.07	0.02	0.04	0.03	0.04
93 +2	0.04	0.04	1.00	0.04	0.07	0.02	0.04	0.03	0.04
94 a	0.04	0.04	0.04	1.00	0.07	0.02	0.04	0.03	0.04
94 b	0.07	0.07	0.07	0.07	1.00	0.04	0.07	0.06	0.07
94 c	0.02	0.02	0.02	0.02	0.04	1.00	0.02	0.02	0.02
95 −2	0.04	0.04	0.04	0.04	0.07	0.02	1.00	0.08	0.10
95 pk	0.03	0.03	0.03	0.03	0.06	0.02	0.08	1.00	0.08
95 +2	0.04	0.04	0.04	0.04	0.07	0.02	0.10	0.08	1.00

Table 4: The experimental correlation matrix for the nine data sets, considering both the statistical and the systematic errors.

Error source	δb ($\times 10^{-5}$)
Photonic corrections	38.
Z interference	30.
Light pairs	11.
Total	50.

Table 5: Estimated theoretical uncertainties on the effective slope b.

Bin	$N_{\rm data}$	$N^0_{\rm MC}$	Ratio $f = N_{\rm data}/N^0_{\rm MC}$	
			anchoring correction	corrected value
1	1310496	1314605	-0.00019	0.99668 ± 0.00087
2	927931	930603	$+0.00082$	0.99795 ± 0.00104
3	941500	938601	-0.00181	1.00128 ± 0.00103
4	431654	430355	$+0.00116$	1.00418 ± 0.00153
5	458295	455712	-0.00032	1.00534 ± 0.00149

Table 6: Detailed inputs to the fit for the largest data subsample (94b). Each row corresponds to a radial bin and gives the number of data events and the number expected from Monte Carlo (normalized to the total number of data events), the applied anchoring correction, and the corrected ratio with its statistical error.

Dataset	$\sqrt{s}$ (GeV)	Number of events	slope b ($\times 10^{-5}$)
93 -2	89.4510	879549	$662 \pm 326 \pm 89$
93 pk	91.2228	894206	$670 \pm 324 \pm 92$
93 $+2$	93.0362	852106	$640 \pm 332 \pm 89$
94 a	91.2354	885606	$559 \pm 326 \pm 86$
94 b	91.2170	4069876	$936 \pm 152 \pm 71$
94 c	91.2436	288813	$62 \pm 570 \pm 122$
95 -2	89.4416	890248	$839 \pm 325 \pm 124$
95 pk	91.2860	581111	$727 \pm 402 \pm 126$
95 $+2$	92.9720	885837	$156 \pm 325 \pm 128$
Average	91.2208	10227352	$726 \pm 96 \pm 70$
χ^2/d.o.f. (stat.)			6.9/8
χ^2/d.o.f. (stat.+syst.)			6.5/8

Table 7: Fit result for each data subsample and average. Each row gives the average centre-of-mass energy, the number of events and the fitted slope b, with the first error statistical and the second the full experimental systematic. The average is obtained by using the error correlation matrix given in Table 4. The χ^2 of the average is given both considering statistical errors only and for the full error matrix.

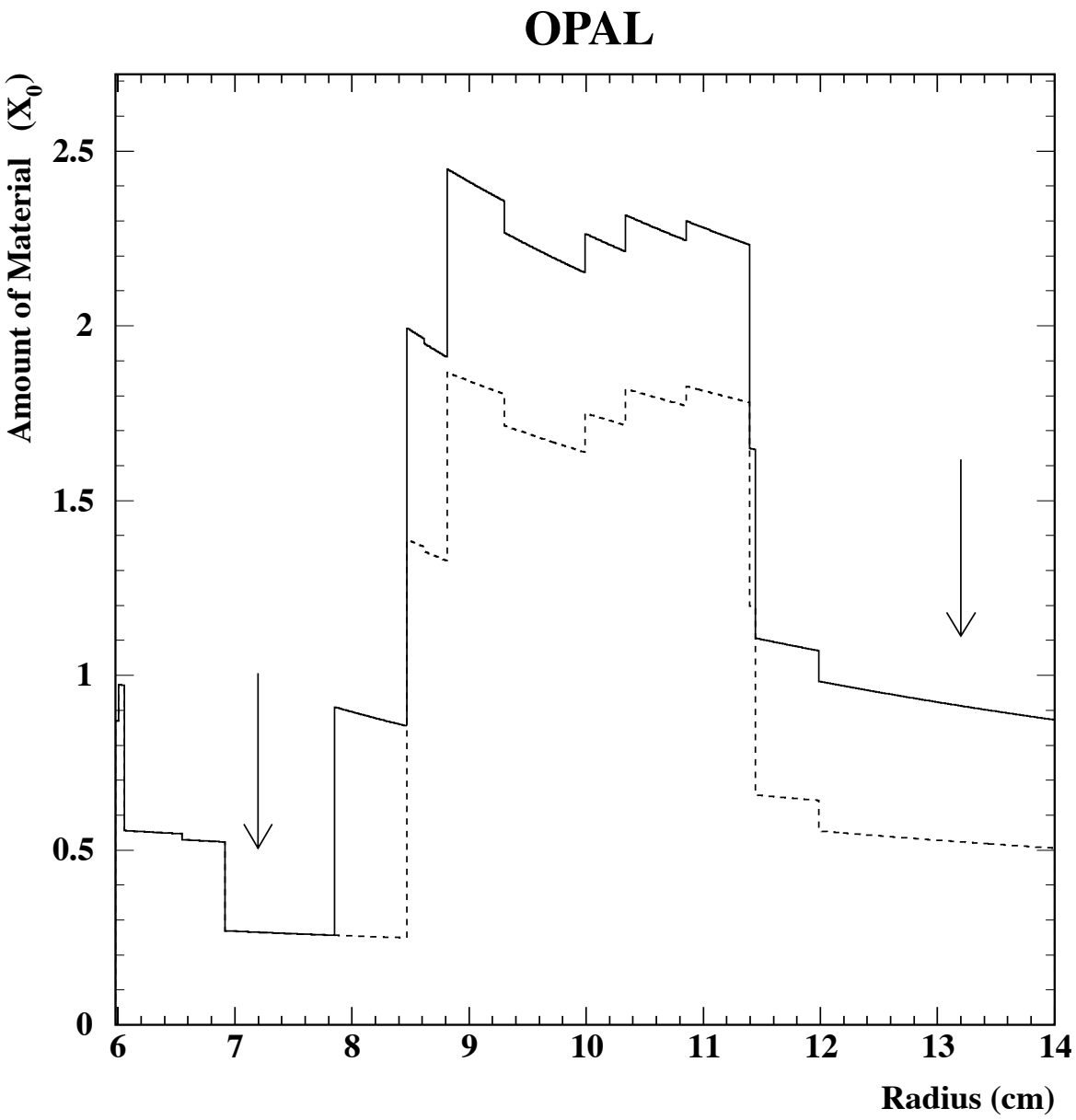

Figure 1: The calculated thickness of material traversed by particles originating at the interaction point as a function of calorimeter radius for the 1993-94 detector configuration. The solid curve corresponds to the Left, the dotted curve to the Right side. The larger amount of material on the Left is due to cables from the OPAL microvertex detector. The arrows show the location of the acceptance definition cuts on shower radius.

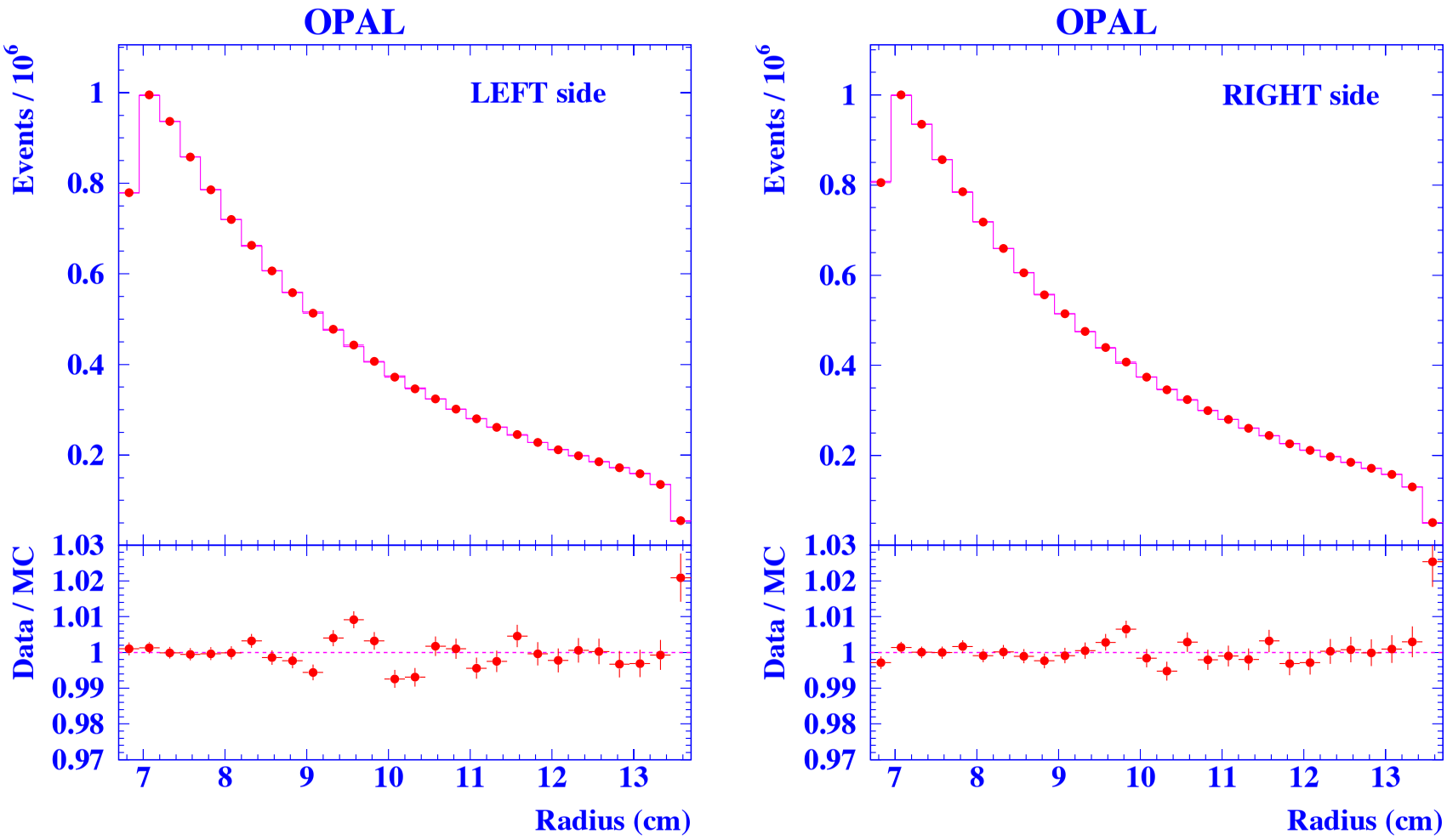

Figure 2: Radial distributions after the isolation cuts for the complete data statistics in the Left and Right calorimeters (mean $\sqrt{s} = 91.2208$ GeV). The points show the data and the histogram the Monte Carlo prediction, assuming the expected running of α, normalized to the same number of events. The lower plots show the ratio between data and Monte Carlo.

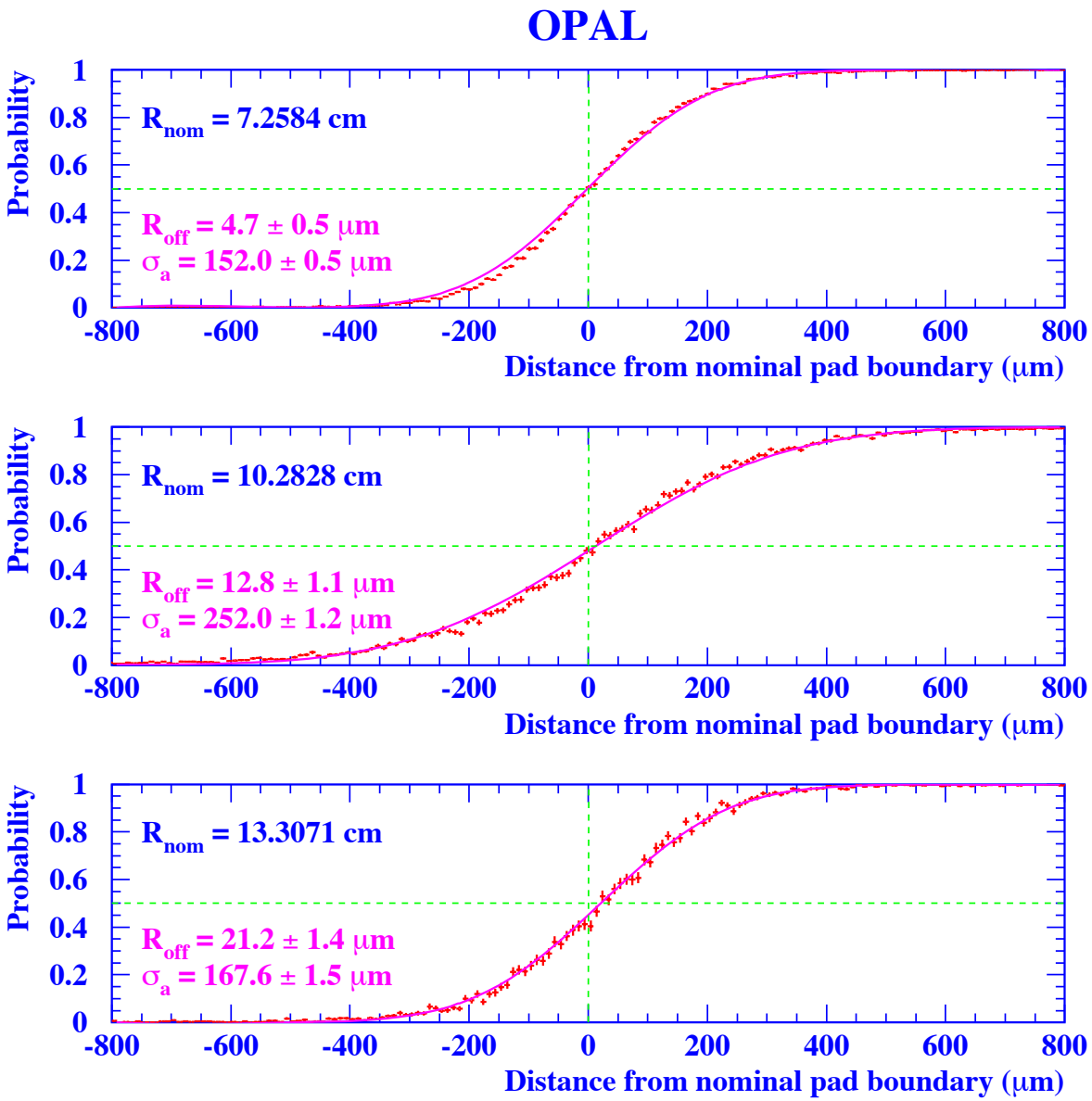

Figure 3: Pad boundary images obtained for the Si layer at $4\,X_0$ at three different radial positions corresponding to the inner edge, the middle portion and the outer edge of the acceptance. The solid curve shows the fitted function, whose parameters $R_{\rm off}$ and $\sigma_{\rm a}$ are given.

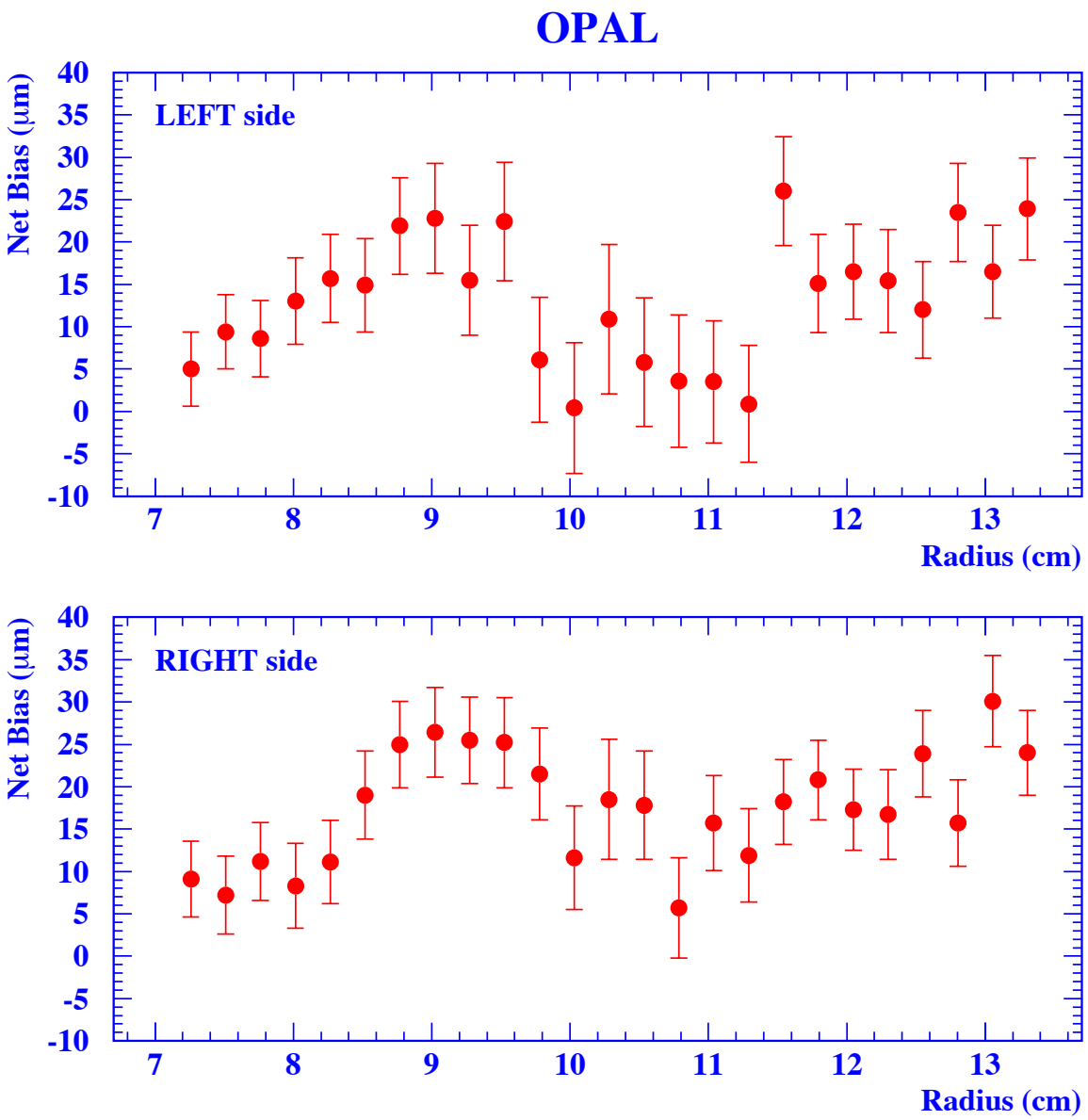

Figure 4: The total net bias δR (anchor) as a function of radius for the Left and the Right radial coordinate determined for the pad boundaries in the Si layer at $4\,X_0$, for the combined 1993-94 data sample. The full error bars show the total error, the inner bars the statistical component where this is larger than the size of the points.

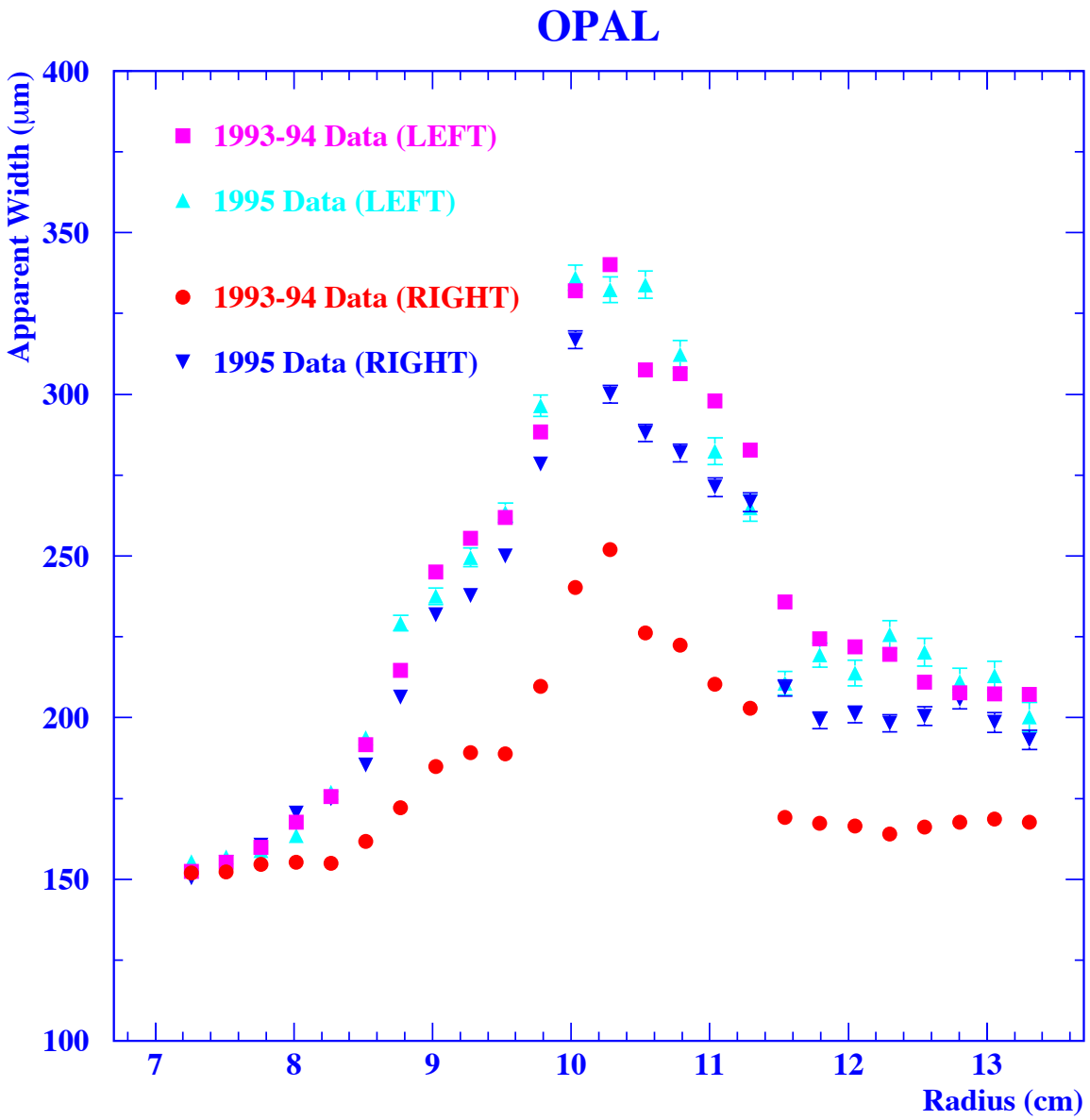

Figure 5: The apparent width σ_a as a function of radius determined from the anchoring procedure for the Si Layer at $4\,X_0$ for homogeneous data subsamples. The errors are statistical only.

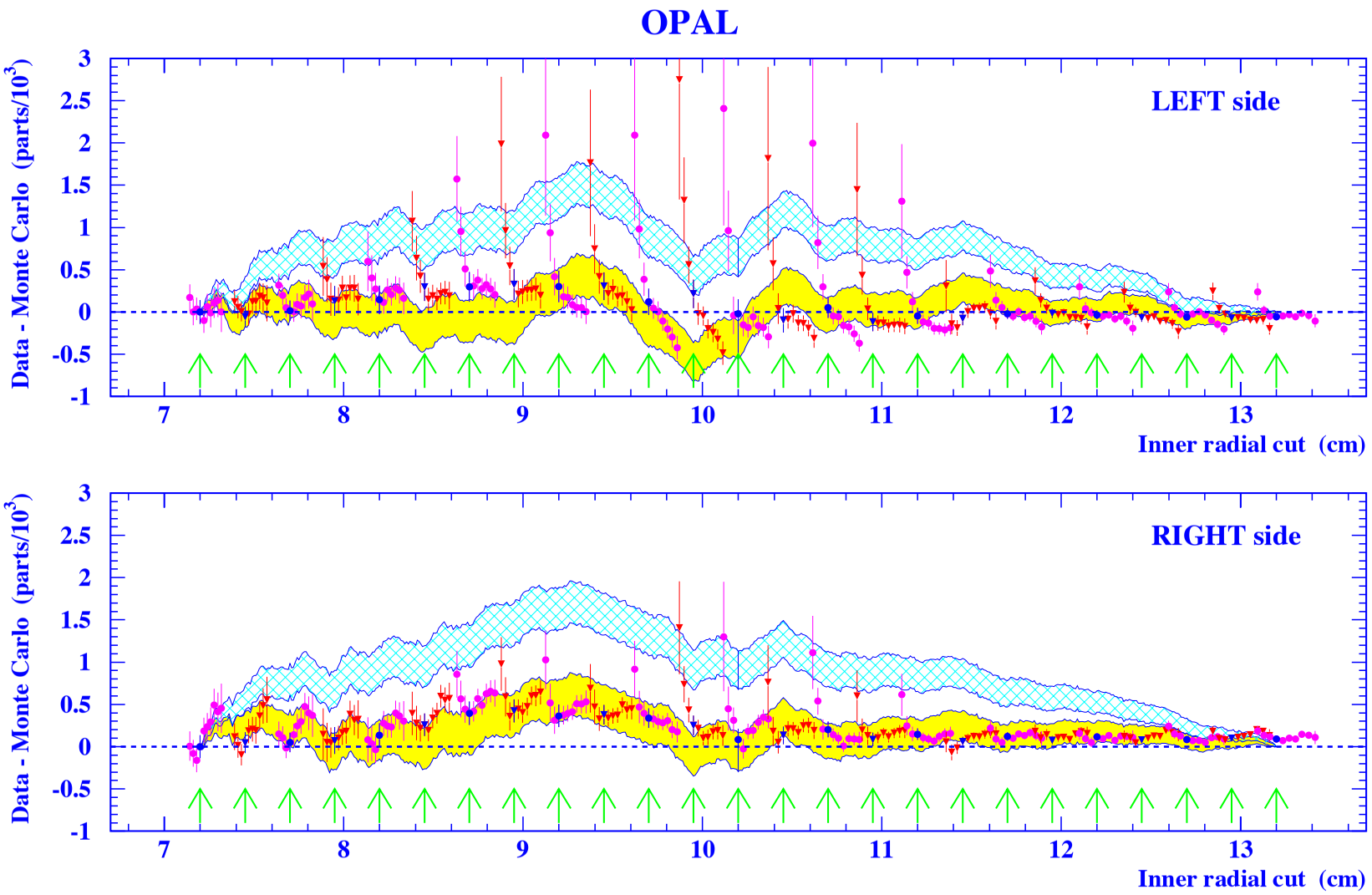

Figure 6: Study of the reconstructed radial coordinate. The shaded band shows the relative change in acceptance between data and Monte Carlo as a function of the definition cut on the inner radius for the combined 1993-94 data sample. The width of the band shows the (highly correlated) statistical errors. The solid points show the acceptance variation determined by the anchoring procedure in Si layers from $1\,X_0$ to $10\,X_0$, with the total errors shown. Triangles and circles designate even and odd rings of radial pads respectively. Within each group of points the arrow shows the location of the radial pad boundary in layer $7\,X_0$, with deeper layers to the left and shallower layers to the right. The anchor at $R = 7.2$ cm is fixed to lie at zero. The hatched band shows the prediction for zero running ($\alpha(t) \equiv \alpha_0$).

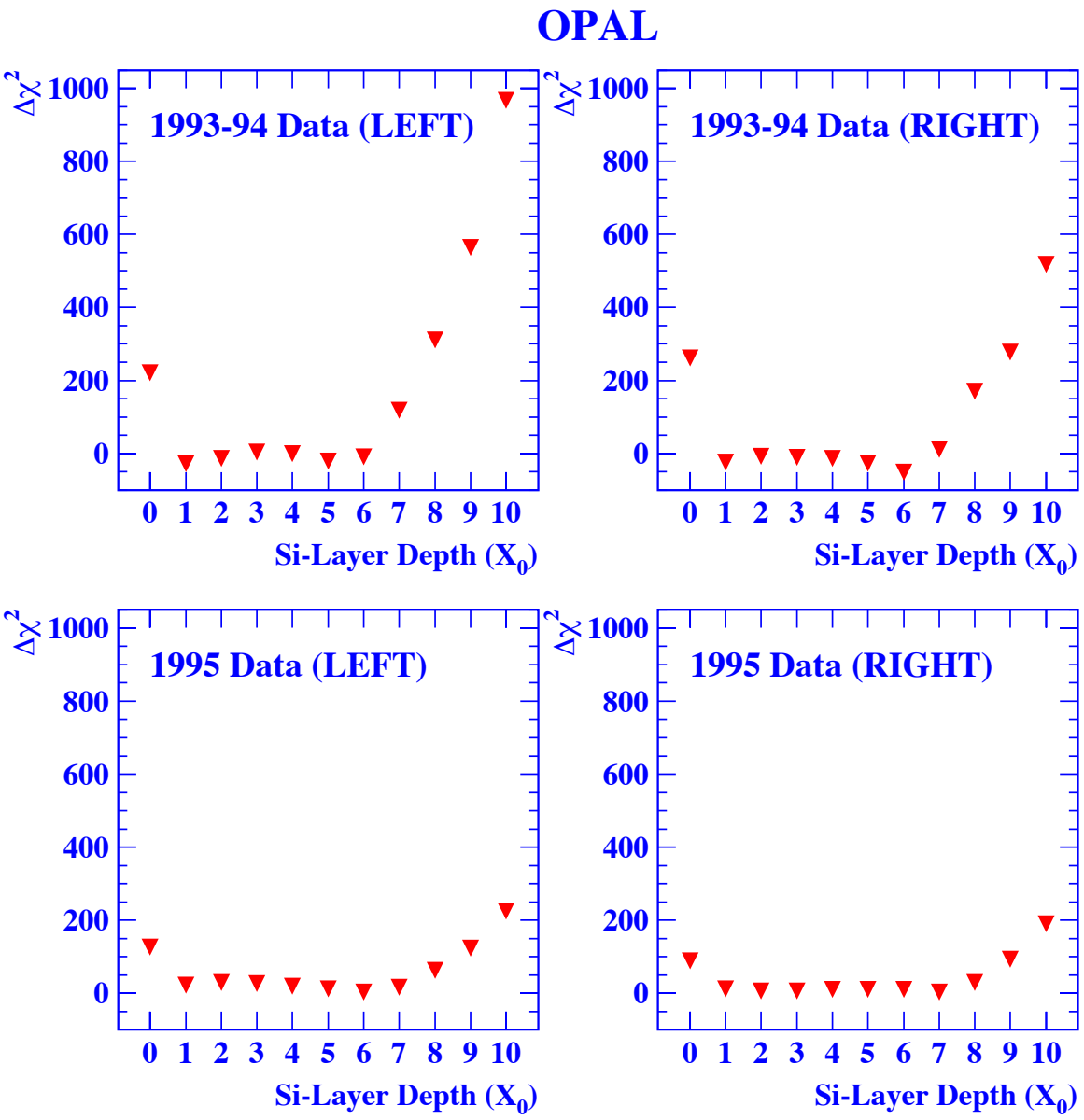

Figure 7: Difference in χ^2 (for 22 degrees of freedom) between the fits of anchored and unanchored radial distributions as a function of the anchoring layer for homogeneous data subsamples. Only statistical errors are considered.

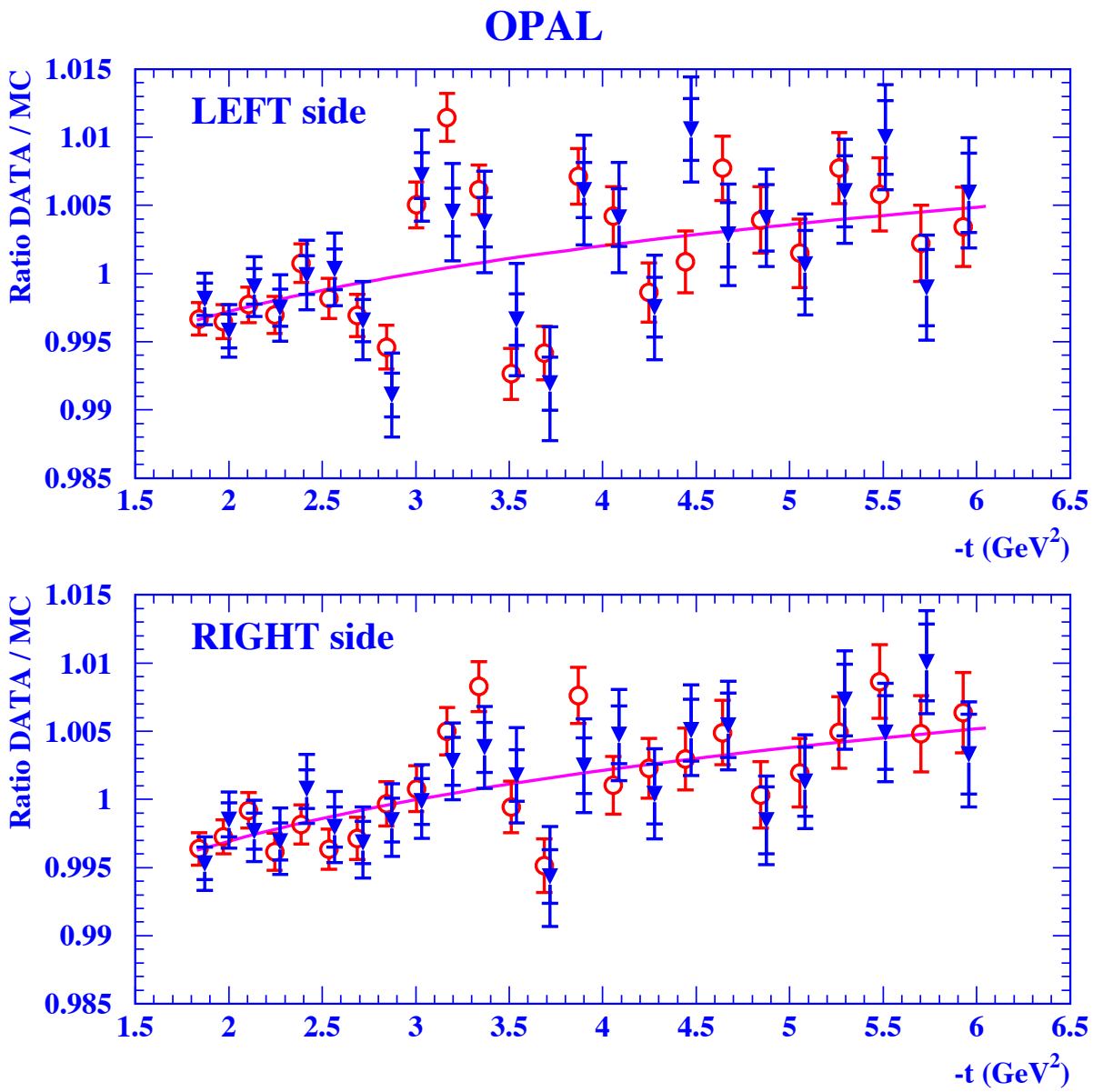

Figure 8: Ratios of numbers of data and Monte Carlo events (with $\Delta\alpha$ set to zero) for the complete data statistics, for the Left and Right sides. Each point corresponds to a bin of one radial pad. The solid triangles show the data corrected with anchors in layer $4\,X_0$, the empty circles the unanchored data (slightly shifted horizontally for clarity), with statistical errors in both cases. The line shows the fit to the anchored data.

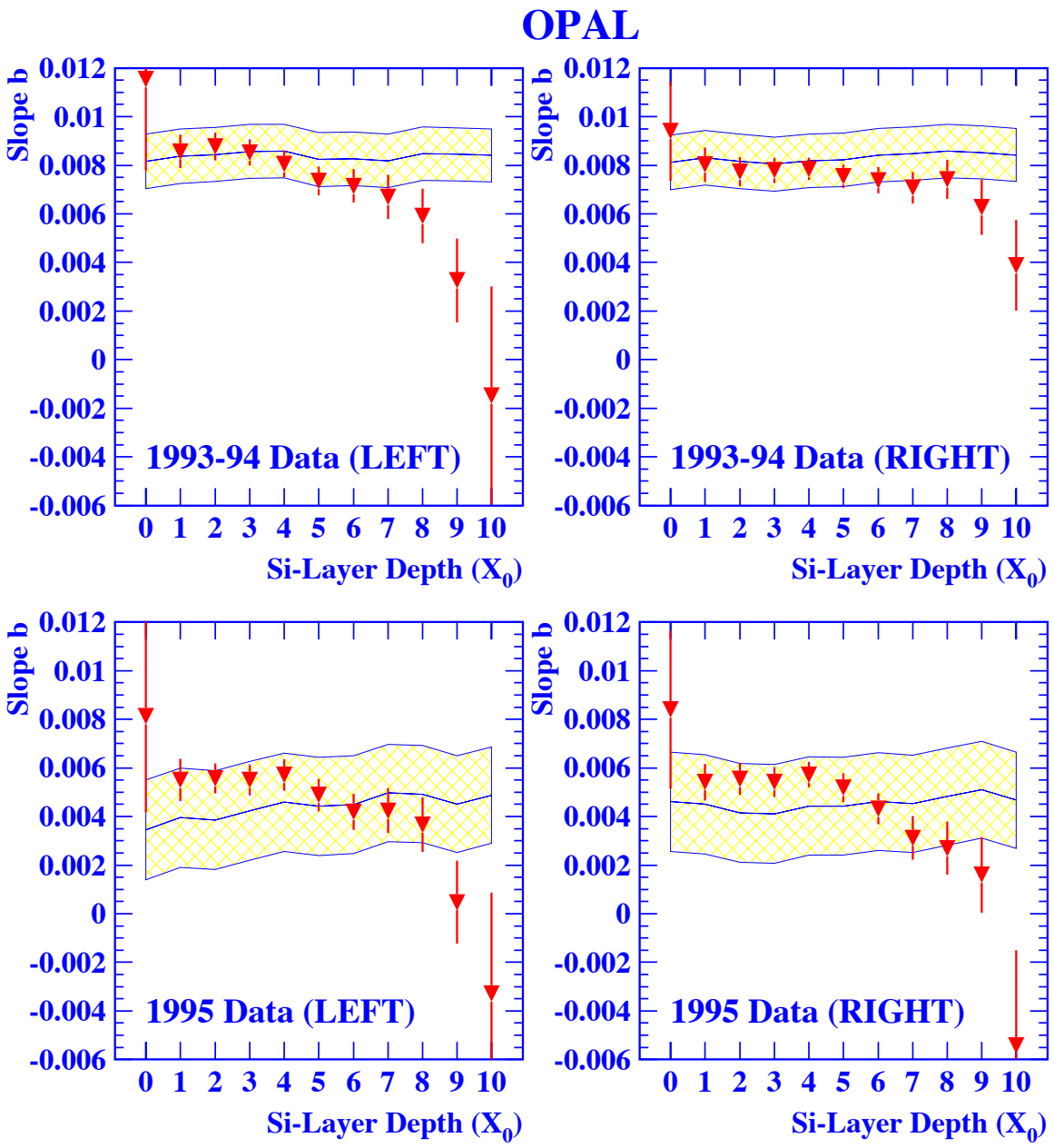

Figure 9: Fitted values of b as a function of the anchoring layer for homogeneous data subsamples. In each case the band shows the result obtained from the unanchored radial distribution, where the width corresponds to the statistical error and the small shifts depend on the rebinning of the distribution in each layer. The solid triangles show results from distributions corrected by anchoring, with the error bars representing only the systematic errors.

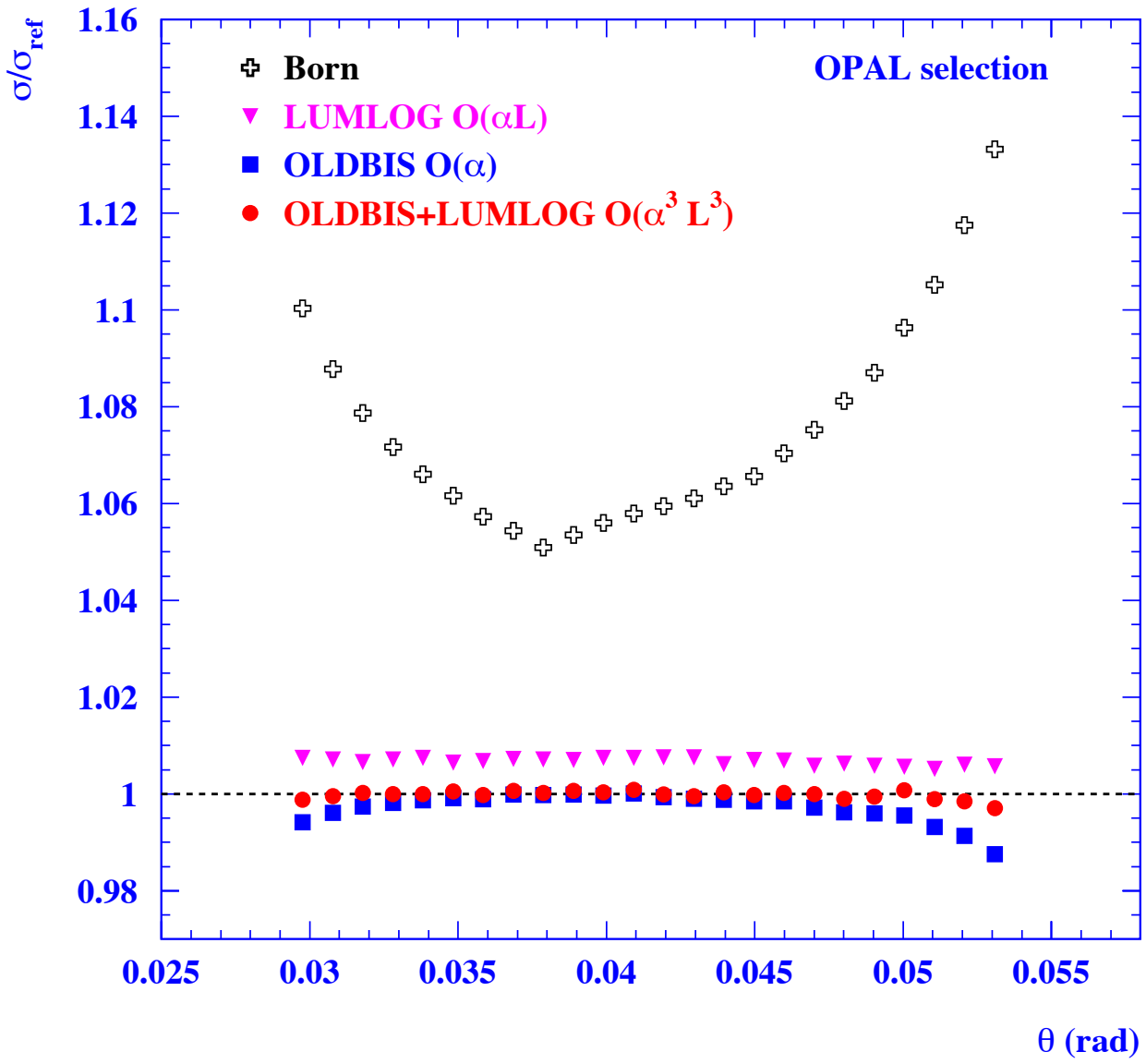

Figure 10: Differential cross section as a function of the polar scattering angle, in different perturbative approximations normalized to the reference BHLUMI calculation, for the OPAL selection. The reference BHLUMI ($\mathcal{O}(\alpha^2 L^2)$ exponentiated) is shown as the dashed horizontal line at $\sigma/\sigma_{\rm ref} = 1$. Vacuum polarization, Z-interference and s-channel photon contributions are switched off.

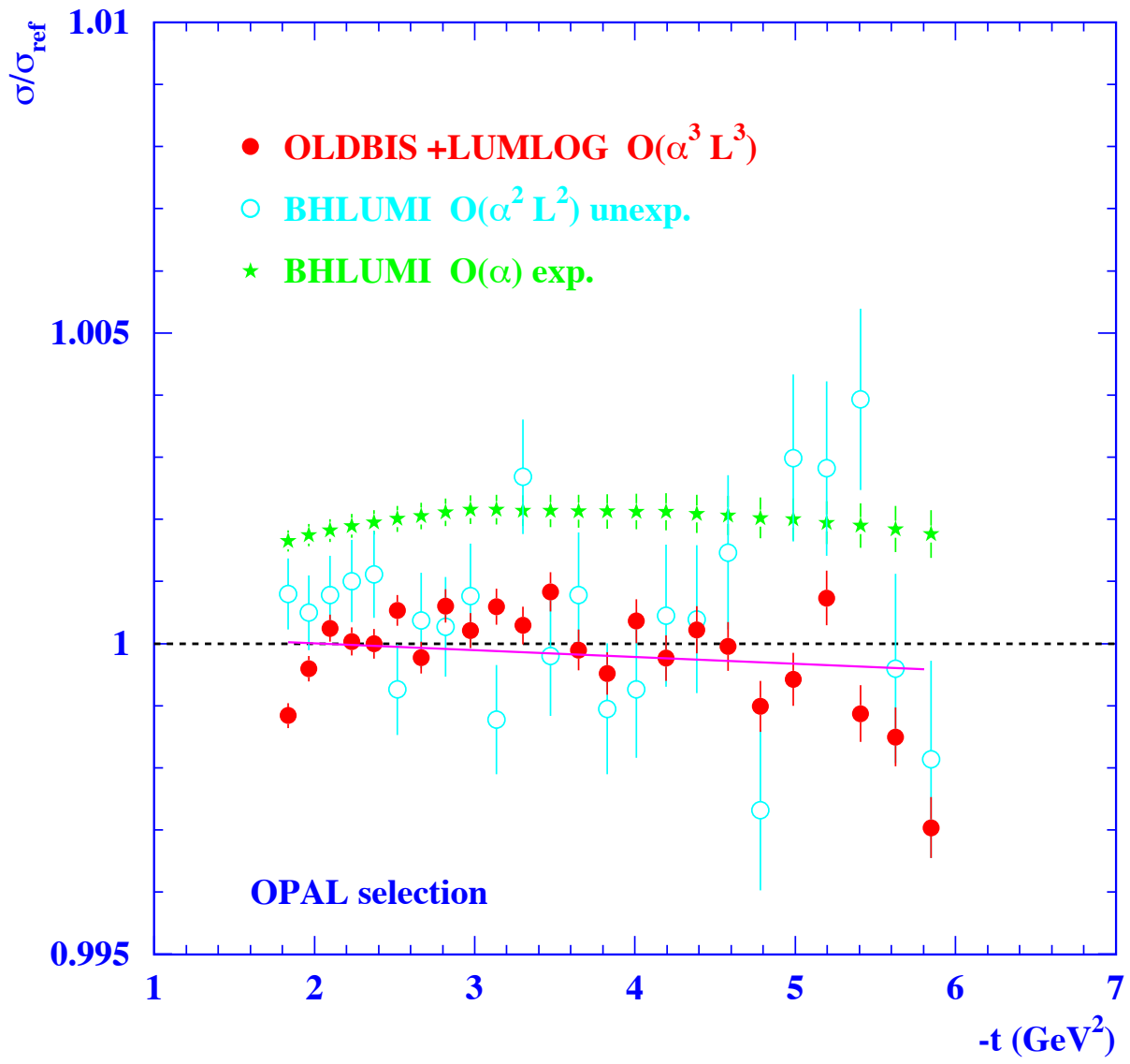

Figure 11: Differential cross section as a function of $-t$, in different perturbative approximations normalized to the reference BHLUMI calculation, for the OPAL selection. The reference BHLUMI ($\mathcal{O}(\alpha^2 L^2)$ exponentiated) is shown as the dashed horizontal line at $\sigma/\sigma_{\rm ref} = 1$. Vacuum polarization, Z-interference and s-channel photon exchange contributions are switched off. The superimposed solid line is a fit to the OLDBIS+LUMLOG result.

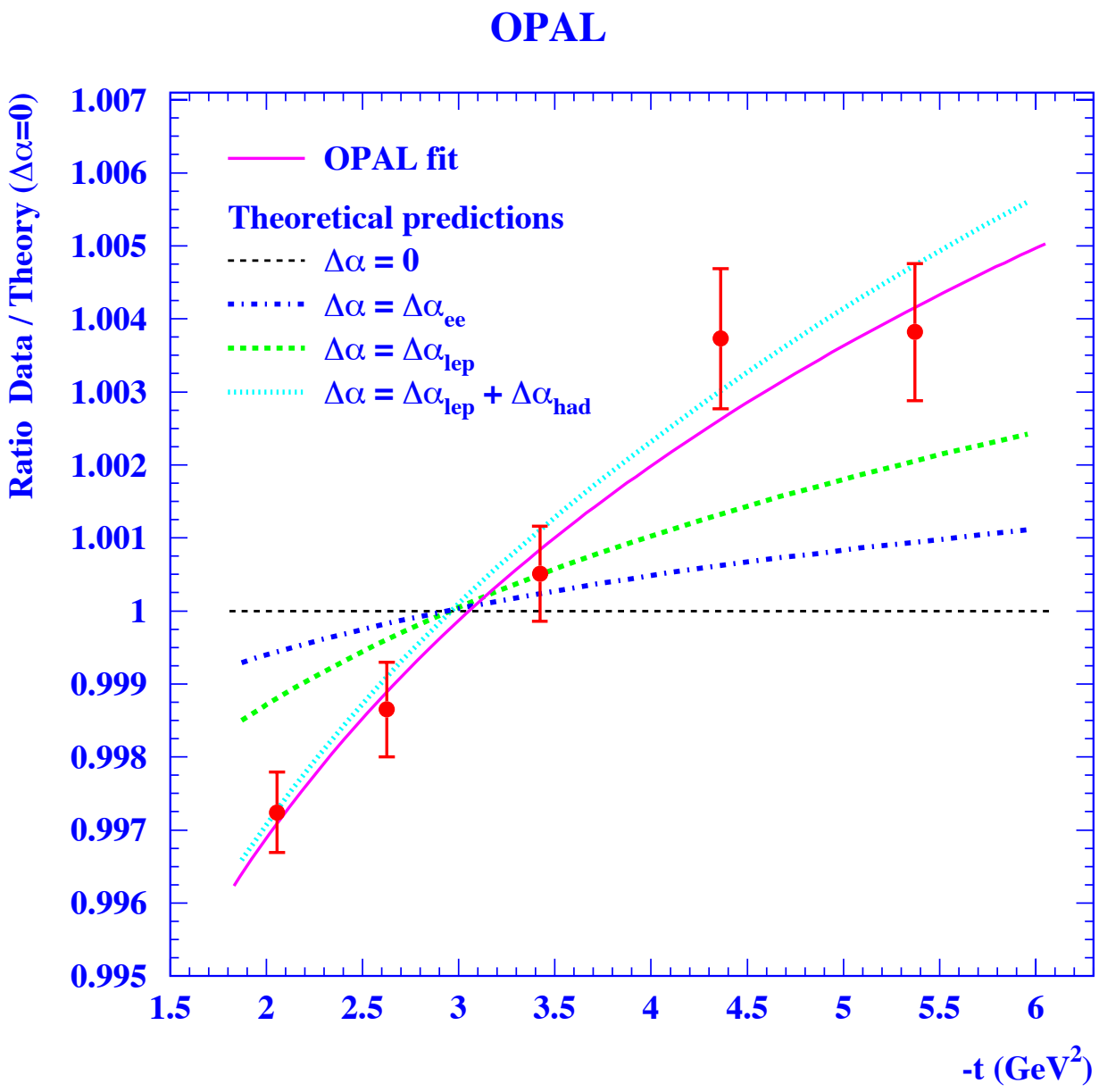

Figure 12: $|t|$ spectrum normalized to the BHLUMI theoretical prediction for a fixed coupling ($\Delta\alpha = 0$). The points show the combined OPAL data with statistical error bars. The solid line is our fit. The horizontal line (Ratio=1) is the prediction if α were fixed. The dot-dashed curve is the prediction of running α determined by vacuum polarization with only virtual e^+e^- pairs, the dashed curve includes all charged lepton pairs and the dotted curve the full Standard Model prediction, with both lepton and quark pairs.